TECHNISCHE UNIVERSITÄT WIEN

Diplomarbeit

On the Redefinition of the Operational Dose Quantities for External Radiation Exposure and its Effect on Practical Radiation Protection

zur Erlangung des akademischen Grades
Diplom-Ingenieur

im Rahmen des Studiums
Technische Physik

eingereicht von
Victor Merza
Matrikelnummer 01426145

ausgeführt am Atominstitut
der Fakultät für Physik der Technischen Universität Wien

unter der Anleitung von
Univ.Prof. Dipl.-Ing. Dr.techn. Franz Josef Maringer
und
Dipl.-Ing. Dr.techn. Christian Hranitzky, MAS

Wien, 19. Mai 2021

Victor Merza	Franz Josef Maringer	Christian Hranitzky

Abstract

The recently published operational dose quantities proposed by the International Commission on Radiation Quantities and Units (ICRU) in ICRU report 95 are defined for the real human body and based on physical field quantities, fluence and air kerma, in contrast to the previous definitions. This should ensure a better estimation of the effective dose. In practical radiation protection, however, measuring instruments intended for this purpose will continue to be calibrated using conventional phantoms such as the ISO water slab. The advantage gained by the redefinition itself could be lost again by passing it on through such phantoms, which is not given much attention in ICRU report 95.

In this thesis, such doubts should be eliminated by simulation and performance of experiments to determine the backscatter factor on the ISO water slab and on an Alderson Rando phantom, or actually existing deficiencies should be shown. The focus is set on the Personal Dose H_{p}, where the particle fluence or air kerma for a point on the body surface is related to the effective dose through a conversion coefficient and is thus related to the backscatter factor.

Measurements of the backscatter factor and of the response of measuring devices on the ISO water slab and on the Alderson Rando phantom were carried out. For this purpose we had a shadow-free design (SFD) ionization chamber, thermoluminescent dosemeters (TLD) and an electronic personal dosemeter (EPD) at our disposal. The Monte-Carlo code MCNP6.2 was used to either simulate the SFD measurements as well as backscatter profiles and spectra. Additionally, simulations of the backscatter factor using the male Adult Mesh-type Reference Computational Phantom (MRCP) were performed.

Results for the backscatter factors were compared, whereby the dependence on the angle of incidence of the radiation and the photon energy was taken into account. Whether the redefinition of the operational dose quantities automatically brings with it the need to develop new measuring devices was discussed.

Zusammenfassung

Die kürzlich von der International Commission on Radiation Quantities and Units (ICRU) im ICRU Report 95 veröffentlichten operativen Dosisgrößen sind, im Gegensatz zu den bisher gültigen Definitionen, auf Grundlage von physikalischen Feldgrößen, der Fluenz und der Luftkerma, und für den realen menschlichen Körper definiert. Dadurch soll eine bessere Abschätzung der effektiven Dosis gewährleistet werden.

Im praktischen Strahlenschutz sollen entsprechende Messgeräte weiterhin an herkömmlichen Phantomen wie dem Wasser-Körper Phantom kalibriert werden. Der an sich gewonnene Vorteil durch die Definition am realen Körper könnte durch die Weitergabe durch solche Phantome wieder verloren gehen, was im ICRU Report 95 nicht sonderlich berücksichtigt wird.

In dieser Arbeit sollten solche Zweifel durch Simulation und Durchführung von Experimenten zur Bestimmung des Rückstreufaktors am Wasser-Körper-Phantom und an einem realistischen Ganzkörperphantom (Alderson Rando) beseitigt werden bzw. tatsächlich vorhandene Mängel aufgezeigt werden. Dabei liegt der Fokus auf der sogenannten Personendosis H_{p}, wo die Fluenz oder Luftkerma an einem Punkt an der Körperoberfläche mittels eines Konversionkoeffizienten mit der effektiven Dosis verknüpft wird und damit eine Beziehung zum Rückstreufaktor aufweist.

Messungen des Rückstreufaktors und der Response von Messgeräten wurden am Wasser-Körperphantom sowie am Alderson Rando-Phantom durchgeführt. Zu diesem Zwecke standen eine schattenfreie Ionisationskammer (SFD), Thermolumineszenzdosimeter (TLD) und ein elektronisches Personendosimeter (EPD) zur Verfügung. Der Monte-Carlo Code MCNP6.2 wurde verwendet um die Messungen mit der SFD zu simulieren und um Rückstreu-Profile und Spektren zu bestimmen. Zusätzlich wurden Simulationen zur Bestimmung des Rückstreufaktors am männlichen Adult Mesh-type Reference Computational Phantom (MRCP) durchgeführt.

Die Ergebnisse für die Rückstreufaktoren wurden verglichen, wobei die Abhängigkeit vom Einfallswinkel der Strahlung sowie von der Photonenenergie betrachtet wurde. Ob die Neudefinition der operativen Dosisgrößen die Notwendigkeit der Entwicklung neuer Messgeräte automatisch mit sich bringt wurde diskutiert.

II:

Glossary

Avogadro constant Number N_A of constituent particles in one mole.
$N_A = 6,02214076 \cdot 10^{23}\ \text{mol}^{-1}$. 6

calibration Activity which, under specified conditions, in a first step determines a relationship between the quantity values provided by standards with their measurement uncertainties and the corresponding indicated values with their measurement uncertainties, and in a second step uses this information to establish a relationship with the aid of which a measurement result is obtained from a display value. i

calibration coefficient Quotient

$$N_X = \frac{M_r}{Q}$$

of the reference value $M_{r,X}$ for a dosimetric quantity, specified by the index 'X', delivered by a standard and the output Q of the measurement device, usually electric current or charge, corrected to reference conditions. 36

calibration factor Quotient

$$N_0 = \frac{M_r}{M_i}$$

of a reference value M_r delivered by a standard and the value M_i indicated by the measurement device, corrected to reference conditions. Coherent SI-unit is 1. 36

charged-particle equilibrium Charged-particle equilibrium at a point exists if the charged-particle fluence rate, differential in energy and direction, is constant within distances equal to the maximum charged-particle range. 18

dosemeter Measuring device for determining a dose and/or dose rate. 35

entrance surface air kerma Air kerma at a point on the surface of an object facing the radiation source produced by the incident radiation as well as backscattered radiation. 10

fluence Differential quotient

$$\Phi = \frac{\mathrm{d}N}{\mathrm{d}A}$$

of the number of particles $\mathrm{d}N$ entering a sphere with cross-sectional area $\mathrm{d}A$ by $\mathrm{d}A$. Coherent SI-unit is m^{-2}. i

focus Point for approximate description of the position of the source of the primary radiation, which is invariably fixed in relation to the mechanical structures of the beam emitter head. 34

ICRU 4-element tissue Tissue-equivalent material with density of 1 g cm^{-3} with mass fractions of 76,2 % oxygen, 11,1 % carbon, 10,1 % hydrogen and 2,6 % nitrogen. 1

ICRU sphere Sphere with a diameter of 30 cm, consisting of ICRU 4-element tissue. 21

linear energy transfer (LET) Differential quotient

$$L_\Delta = \left(\frac{\mathrm{d}E}{\mathrm{d}s}\right)_\Delta$$

of the mean energy loss $\mathrm{d}E$ of a charged particle of energy E by its path length $\mathrm{d}s$ due to collisions in a material during which the energy transfer of a secondary particle liberated through an ionization process is smaller than Δ, or solely an excitation is effected. Coherent SI-unit is J m^{-1}. 21

measurement standard Measuring system, dimensional standard or reference material with the purpose of realizing the definition of a quantity and calibration of other standards or measuring devices. 34

molar mass Mass of one mole of a chemical compound. 6

mole SI-unit for the amount of substance, symbol is mol. One mole consists of $6,02214076 \cdot 10^{23}$ particles. 6

nuclide class of atoms characterized by the composition of the atomic nucleus consisting of a certain number of protons (atomic number), Z, and a number of neutrons, N. 73

particle flux density or particle fluence rate; Differential quotient

$$\dot{\Phi} = \frac{\mathrm{d}^2 N}{\mathrm{d}A \cdot \mathrm{d}t} = \frac{\mathrm{d}\,\Phi}{\mathrm{d}t}$$

where $\mathrm{d}^2 N$ is the number of particles, which enter a sphere with cross-sectional area $\mathrm{d}A$ per time interval $\mathrm{d}t$, where Φ is the fluence. Coherent SI-unit is $\mathrm{m}^{-2}\ \mathrm{s}^{-1}$. 5

phantom Object that physically replicates a human or animal body or part thereof in such a way that it behaves, to a sufficient degree of approximation, like the body or its part in a diagnostic, therapeutic, or dosimetric procedure. 35

radiation protection Protection of the life or health of people, including their offspring, from harm caused by ionizing radiation. i

radiation quality Parameter with the purpose of classification of the relative spectral particle flux density of radiation in a point of interest. A complete specification of the radiation quality includes an indication of the type of radiation and its energy distribution. 19

radionuclide Radioactive or unstable nuclide 73

response Quotient

$$R = \frac{M_\mathrm{i}}{M_\mathrm{r}}$$

of the indicated value M_i and a reference value M_r for the measured quantity under specified conditions. The relative response r is given by the quotient

$$r = \frac{R}{R_0}$$

of the response R of the measuring device and the reference response R_0, which is the response for reference conditions. i

rest energy Energy E of a stationary particle given by

$$E = mc^2$$

according to the equivalence of mass and energy. m is the rest mass of the particle and c is the speed of light. 17

rest mass invariant mass; Newtonian mass measured of an object resting in the system of the observer 7

traceability Property of a measurement result or the quantity value of a standard to be related to suitable standards, generally national or international standards, by an unbroken chain (calibration chain) of comparative measurements with stated measurement uncertainties. 34

Descriptions in the glossary are mostly taken from [1].

Contents

Chapter 1

Introduction

In radiation protection, there are two fundamental groups of quantities that are used in complementary way to estimate the stochastic risk for harmful effects on the human organism due to external exposure to ionizing radiation.

On the one hand, the International Commission on Radiological Protection (ICRP) published the so-called protection quantities and recommends their use. These quantities related to the human body are defined for extended volumes of a special tissue, for example an organ, and are therefore not measurable by their nature. The risk regarding the occurrence of deterministic effects due to external radiation exposure is assessed by organ equivalent dose, and effective dose is used to estimate the risk for stochastic effects like cancer induction. Protection quantities are thus used to set dose-limits to prevent health effects of ionizing radiation.

On the other hand, the International Commission on Radiation Quantities and Units (ICRU) defines the so-called operational dose quantities, which represent a measurable point quantity. They are suitable for the calibration of measuring instruments for area monitoring and personal dosemeters and should provide an estimate for the protection quantities (Fig. 1.1).

However, strong discrepancies were found between the protection quantities and their estimate by operational dose quantities for very low (< 50 keV for photons) as well as for very high (> 5 MeV for photons) particle energies. Beside others, this was a reason for the redefinition of these quantities in order to obtain a better estimation of the protection quantities, which were finally published at the end of 2020 in the ICRU Report 95 'Operational Quantities for External Radiation Exposure' [2]. The new definition also included an extension to a number of different particles, whereas in the previous definition only photons, neutrons and electrons were considered.

So far, use has been made of the ICRU 4-element tissue with a density of 1 g cm^{-3}, which represents a tissue equivalent. For example, the personal dose equivalent

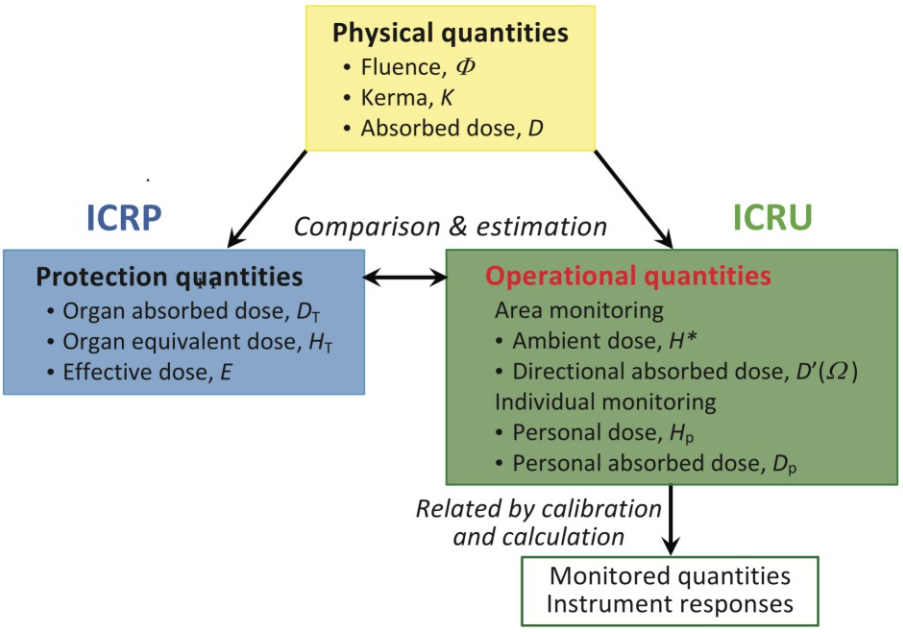

Figure 1.1: Scheme of the interrelationships between the physical quantities which are the basis for the protection quantities proposed by the ICRP and the operational quantities recently proposed by the ICRU [2].

$H_p(10)$, $H_p(3)$ and $H_p(0,07)$ is defined in ICRU 4-element tissue as the dose equivalent in a depth of 10 mm, 3 mm and 0,07 mm, respectively, below a certain point on the human body corresponding to the protection quantity which is supposed to be assessed. $H_p(10)$ serves as estimate for effective dose, $H_p(3)$ for the equivalent dose in the lens in the eye, and $H_p(0,07)$ for the equivalent dose in local skin [3, 4].

It is of essential importance that the new operational quantity, the so-called personal dose H_p, which replaces the mentioned previous personal dose equivalents, is no longer defined in a certain depth in ICRU 4-element tissue, but at the surface of the uniformly irradiated body. In addition, a transition is made to radiometric field quantities, namely air kerma and fluence in combination with a conversion coefficient, which brings an additional difference to the previous definition where absorbed dose in combination with a LET-dependent quality factor in tissue was used for the calculations [2]. Despite these significant changes, the current method of calibrating dosimeters is recommended to remain the same. To take the personal dose as an example, calibration here will continue to be performed on the ISO water slab, since it is assumed that this phantom is a sufficiently good representation of the human body as it is for $H_p(10)$. Corresponding calculations have not yet been performed for H_p, which was the basic motivation of this work. The aim of this thesis is to confirm the applicability of the ISO water slab as calibration phantom

for the new operational dose quantity, personal dose H_p – or otherwise to show a serious deficiency of this concept.

One opportunity to determine whether the ISO slab actually represents the human body sufficiently well is to compare the backscattering on this phantom with the backscattering on an anthropomorphic phantom. The different shape and material composition could lead to discrepancies in the dose a dosemeter measures on the surface of the corresponding phantom due to differently backscattered radiation. Regarding the definition of H_p, which is defined for a point on the surface of the body, the connection to the backscatter factor is automatically found here, which can be estimated by measurements using suitable detectors and by performing Monte Carlo simulations.

What will have far-reaching consequences in any case is that, as a result of the redefinition of the operational dose quantities, the currently approved dose measuring devices may not be able to be simply calibrated to the new quantities. Depending on the operation mechanisms of the dosemeters, some of them will no longer be able to meet the legal requirements, which would require dosemeter modification or redesign to meet the requirements of international standards. Thus, once the new quantities are incorporated into the legislation, there will be implications for users as well as manufacturers of dosemeters.

Chapter 2

Theory

2.1 Ionizing Radiation

Radiation that has the ability to detach electrons from the atoms of a material with which the radiation interacts is called ionizing radiation. Thereto, a minimum energy which is equal to the binding energy of the loosly bound electrons in the outer atomic shell is necessary. Depending on the irradiated material, this energy is approximately between 10^{-19} J and 10^{-16} J.

A distinction in two classes of ionizing radiation can be made depending on the mechanism to which most ionizations are due. Directly ionizing radiation consists of massive charged particles (electrons, protons, alpha particles etc.) and interacts with the electrons in the atomic shell through the coulomb force and leads to immediate ionization. In contrast, electrically neutral particles (neutrons, photons), whose interaction probability with matter is generally lower, belong to the indirectly ionizing radiation. Here, the majority of ionization events is due to ionizations through charged secondary particles.

X-rays are photons or rather electromagnetic waves with maximum wavelengths of about 10 nanometers corresponding to an energy of 124 eV. Due to their ability to expel electrons from the atomic shell of an atom, X-radiation is ionizing radiation and belongs to the class of indirectly ionizing radiation, whereby they differ from gamma rays solely in their origin. Gamma rays are generated during radioactive decays of atomic nuclei whereas X-rays arise from changes in the velocity of charged particles or from electronic transitions in the atomic shell [5, 6].

2.2 Interaction of X-Rays with Matter

2.2.1 Cross Section

The cross section σ determines the probability for an interaction of a photon beam with an absorber. σ may be given with regard to a single electron, σ_e, or atom, σ_a, and is then designated as 'cross section per electron' or 'per atom'. The cross sections with indices 'e' or a' may not be confused with the photon interaction coefficients discussed in the following section, which are usually also represented by the greek letter σ with corresponding indexing.

The cross section σ with the dimension of an area represents the effective area that an incoming photon incident on an atom or atomic nucleus sees. A commonly used unit is 1 barn = 1 b = 10^{-28} m^2 = 10^{-24} cm^2. The larger σ, the larger the probability for the interaction for the regarding process. Especially for photons, the interaction cross section does not correspond to the geometric cross section in general. In quantum mechanics, the easily imaginable interpretation of σ as an cross sectional area fails, which is why the cross section in quantum mechanical systems is defined as the ratio of the rate R of a certain type of reactions per unit time and per center of reaction (atomic nucleus, for instance) and the particle flux density j of the incident particles (particles per area and unit time):

$$\sigma = \frac{R}{j} \tag{2.2.1}$$

For certain calculation, the cross section σ_e per electron rather than the cross section per atom is of interest, for example for the quantitative description of the Compton effect. The electronic cross section is then determined by the atomic cross section σ_a divided by the number of electrons, which is equal to the atomic number Z, the number of protons in the atomic nucleus:

$$\sigma_e = \frac{\sigma_a}{Z} \tag{2.2.2}$$

For quantitative studies of scattering, the differential cross section $\frac{\sigma}{\Omega}$ with regard to the solid angle Ω (or scattering angle) is of interest. It is given by the ratio of the number of photons scattered in a certain solid angle element $d\Omega$ per unit time and reaction centers, and the flux density of the incident photons. Differential cross section can also be given with regard to the energy of the emitted particles (spectral differentiating) or to the angle as well as the energy. This description is valid for microscopic processes.

Making the step to a macroscopic description of interaction processes and the resulting attenuation of a photon beam, attenuation coefficients μ are defined. The connection between the attenuation coefficient and the microscopic atomic cross section can be described as follows. For a certain material, the atomic density n_a is given by the number of atoms N_A per mole (Avogadro constant) and the molar mass M_A:

$$n_\mathrm{a} = \frac{N_\mathrm{A}}{M_\mathrm{A}} \tag{2.2.3}$$

The product of n_a and the atomic cross section σ_a defines the interaction cross section per mass unit, which is identical to the definition of the mass attenuation coefficient $\frac{\mu}{\rho}$:

$$\frac{\mu}{\rho} = n_\mathrm{a} \cdot \sigma_\mathrm{a} = \frac{N_\mathrm{A}}{M_\mathrm{A}} \cdot \sigma_\mathrm{a} \tag{2.2.4}$$

leading to an expression for the linear absorption coefficient

$$\mu = \rho \cdot n_\mathrm{a} \cdot \sigma_\mathrm{a} = \rho \cdot \sigma_\mathrm{a} \cdot \frac{N_\mathrm{A}}{M_\mathrm{A}} \tag{2.2.5}$$

which gives the attenuation of a narrow radiation beam per length unit [5].

2.2.2 Scattering

2.2.2.1 Coherent (Thomson) Scattering

We consider a single free electron which represents the scattering object for an incident X-ray. According to classical electrodynamics, the electric field of the X-ray exerts force on the electron carrying electric charge leading to an oscillation of the electron. The accelerated electron hereafter radiates an electromagnetic wave itself. The wavelength of that emitted wave is the same as that of the incident wave and thus no net momentum transfer on the electron takes place. This process is called elastic (Thomson) scattering or coherent scattering [6]. The differential scattering cross section for coherent scattering on an electron with an unpolarized source is determined by the classical electron radius r_0 and the scattering angle ψ by

$$\frac{\mathrm{d}\sigma_\mathrm{coh}}{\mathrm{d}\Omega} = \frac{r_0^2}{2} \cdot \left(2 - sin^2\psi\right) \tag{2.2.6}$$

2.2.2.2 Inelastic (Compton) Scattering

When energy is transferred to the electron in the situation described above the collision is an inelastic scattering process (Compton scattering). Here, a classical

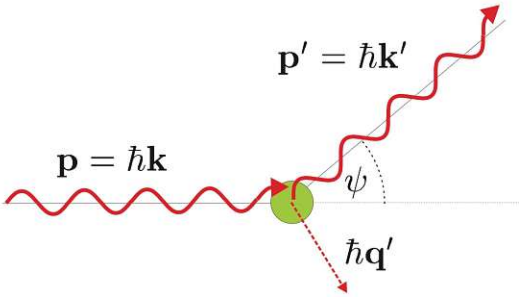

Figure 2.1: Illustration of the Compton effect. The incoming photon is scattered inelastically on a resting electron by the scattering angle ψ and subsequently propagates with reduced photon energy due to the energy transfer to the electron [6].

description fails so we have to switch to a quantum mechanical description.

For simplicity, we assume a resting single free electron with its well known rest mass of $mc^2 = 511$ keV. This represents a good approximation for weakly bound electrons in the outer shell of an atom. An incoming photon with momentum $\vec{p} = \hbar\vec{k}$ and wavelength λ collides with the electron which thereupon receives a momentum of $\hbar\vec{q'}$ and subsequently propagates as a 'recoil' electron. The angle between the initial momentum $\vec{p}$ of the incoming photon and the momentum $\vec{p'}$ of the scattered photon with wavelength λ' is the scattering angle ψ (Fig. (2.1). Considering the conservation of energy

$$mc^2 + \hbar ck = \sqrt{(mc^2)^2 + (\hbar cq')^2} + \hbar ck' \tag{2.2.7}$$

and conservation of momentum

$$\vec{q'} = \vec{k} - \vec{k'} \tag{2.2.8}$$

the following relation between the wavelengths λ and λ' or energies E and E' of the incoming or scattered photon and the scattering angle ψ can be derived:

$$\frac{\lambda'}{\lambda} = \frac{E}{E'} = 1 + \lambda_C k(1 - cos\psi) \tag{2.2.9}$$

The quantity λ_C is the Compton wavelength of the particle involved defined by

$$\lambda_C = \frac{\hbar}{mc} \tag{2.2.10}$$

which represents the wavelength of a photon whose energy is equal to the rest mass mc^2 of the particle [6]. In Fig. 2.2, the ratio $\frac{E'}{E}$ as a function of the scattering angle is calculated from Equ. 2.2.9 exemplary for a photon colliding with a free resting

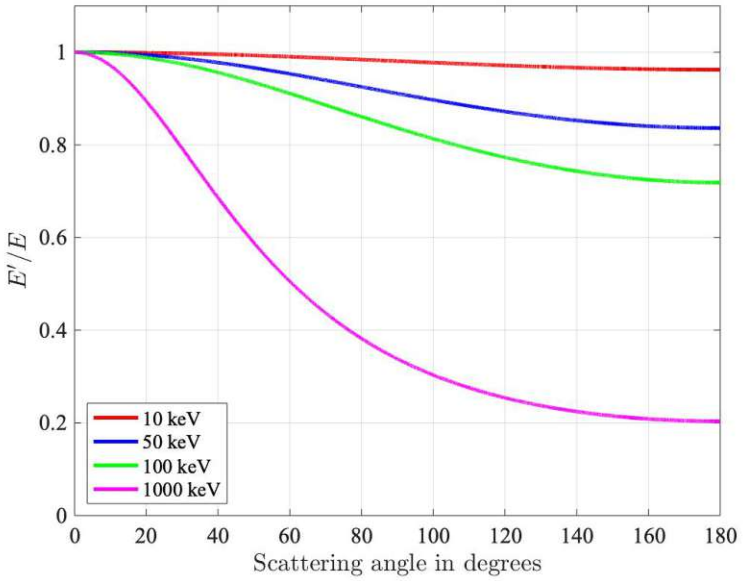

Figure 2.2: Ratio $\frac{E'}{E}$ of energy E' of the scattered photon on an electron to the energy E of the incident photon as a function of the scattering angle.

electron.

For an incident photon, the probability that the Compton effect occurs is determined by the Compton-cross section σ_{C} which can be split into the scattering coefficient σ_{scat} for the incoherent photon scattering and the energy transfer coefficient σ_{tr} for the energy transfer to the detached electron [5–7]:

$$\sigma_{\mathrm{C}} = \sigma_{\mathrm{scat}} + \sigma_{\mathrm{tr}} \tag{2.2.11}$$

For the calculation of the Compton cross section, relativistic quantum mechanical methods are necessary. This was first done by *Klein* and *Nishina* which derived the so called Klein-Nishina formula for the Compton effect delivering collision, scattering and transfer cross sections and their angular distributions of photons scattered on electrons. The Klein-Nishina formula for the electronic differential collision cross section $\mathrm{d}\sigma_{\mathrm{C}}/\mathrm{d}\Omega$ is

$$\frac{\mathrm{d}\sigma_{\mathrm{C}}}{\mathrm{d}\Omega} = \frac{r_0^2}{2} \cdot \left(\frac{E'_\gamma}{E_\gamma}\right)^2 \cdot \left(\frac{E'_\gamma}{E_\gamma} + \frac{E_\gamma}{E'_\gamma} - sin^2\psi\right) \tag{2.2.12}$$

For small photon energies, scattering becomes increasingly coherent and the Compton cross section transforms to the Thomson cross section [5].

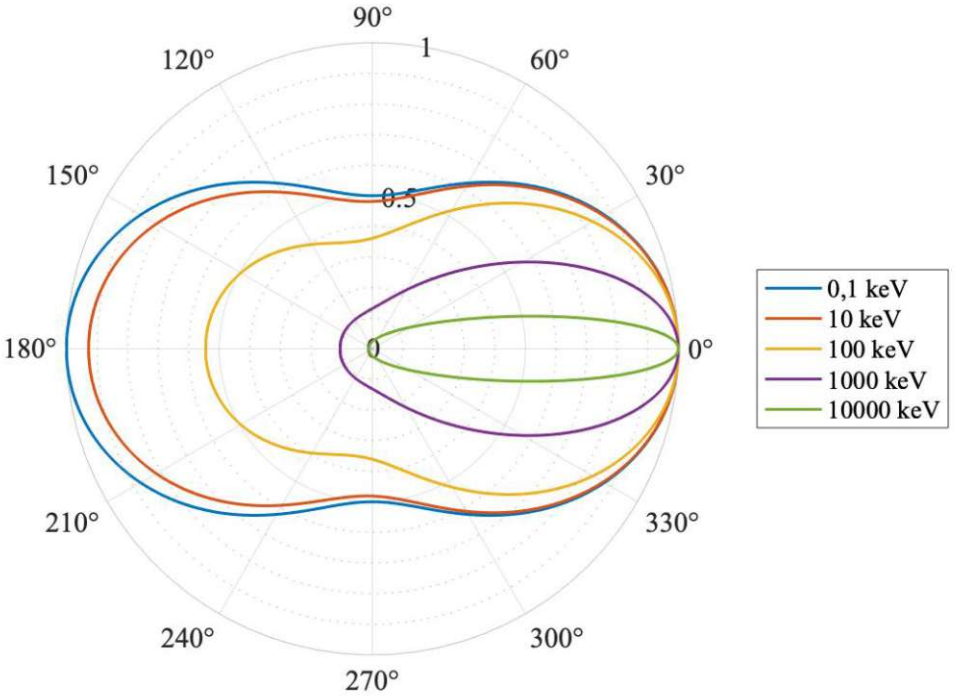

Figure 2.3: Relative angular distribution of the differential Compton-scattering cross section for photons incident from 0°, calculated using the Klein-Nishina formula (Equ. 2.2.12.)

2.2.3 Backscatter Factor

Considering Fig. 2.3, all photons scattered by an angle greater than 90° are called backscattered. The backscatter factor B is defined as the ratio of a dose quantity (discussed in detail in the following sections) like air kerma $K_{\mathrm{a}}^{\mathrm{ph}}$ at a point on the surface of an object facing a radiation source and the dose quantity at the same position free-in air, air kerma K_{a}:

$$B = \frac{K_{\mathrm{a}}^{\mathrm{ph}}}{K_{\mathrm{a}}} \tag{2.2.13}$$

The object can be a human patient, a calibration phantom or any other object from which the backscatter factor could be of interest. This is the definition which was assumed in this work.

In literature there are also some differing definitions present. According to [8], the backscatter factor is given by the ratio of the water kerma at the surface of a phantom to the water kerma at the same point in absence of the phantom. In both cases, the considered point lies on the beam axis. According to [9], the backscatter factor is given by the ratio of the entrance surface air kerma to the air kerma produced solely by the incident radiation.

2.2.4 Absorption

2.2.4.1 Photoelectric Absorption

When an X-ray photon with energy $h\nu$ is completely absorbed by an electron in the atomic shell, an excess of energy that may be available can lead to ionization of the atom since the electron in the atomic shell overcomes the binding energy E_{n} to the shell with principal quantum number n and is emitted with a certain kinetic energy E_{kinetic} (Fig. 2.4). The atomic shells are named with increasing principal quantum number with the letters K for n=1, L for n=2 (and further in alphabetical order). The energy balance in this case is given by

$$h\nu = E_{\mathrm{n}} + E_{\mathrm{kinetic}} \tag{2.2.14}$$

The binding energy for a certain shell is characteristic for the element. After the photoelectric absorption process, the atom remains in single ionized state with an unoccupied hole in its shell [5–7].

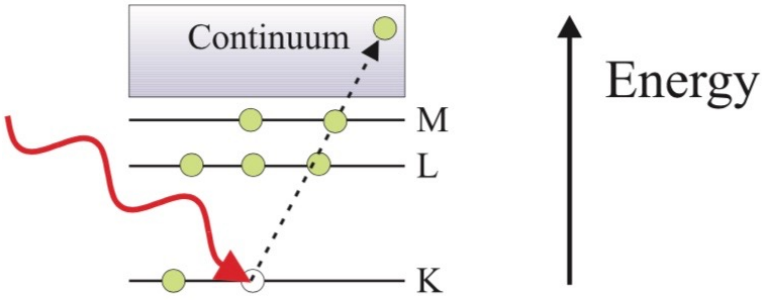

Figure 2.4: Illustration of the photoelectric effect. An incoming photon (red arrow) transfers its total energy to an electron (green dot) in the K-shell which is subsequently expelled from the atom [6].

2.2.4.2 Fluorescence

A hole in an inner shell with principal quantum number n represents an energetically more favorable state for an electron in an higher shell with principal quantum number $m > n$ due to its higher binding energy. From the transition of the electron from a higher shell with binding energy E_m to a hole in the lower shell with E_n, the excess of energy due to the difference in their binding energies can be emitted as a photon with energy

$$h\nu_\mathrm{f} = E_\mathrm{m} - E_\mathrm{n} \tag{2.2.15}$$

Photons resulting from a transition to the K-shell, for instance, are denoted as K_α, K_β etc. with indices corresponding to the shell from which the electron originates (L, M etc.). The emission of this radiation is called fluorescence and is characteristic for every element (Fig. 2.5) [5–7].

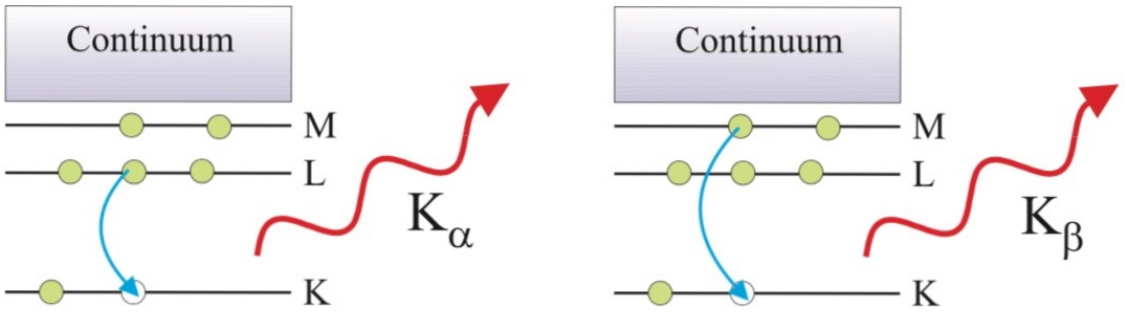

Figure 2.5: Illustration of the fluorescence. An electron (green dot) originating from the L-shell (left) or from the M-shell (right) fills a hole in the K-shell, the excess energy is emitted as a characteristic K_α or K_β photon [6].

2.2.4.3 Auger Effect

Competetive to the emission of fluorescence radiation, the energy released during the transition of the electron from the higher shell with E_m to the hole in the lower shell with E_n can be transferred to an electron in an even higher shell with binding energy $E_\mathrm{l} < E_\mathrm{m} < E_\mathrm{n}$ which is then expelled from the atom (Fig. 2.6). In contrast to the photoelectric absorption, this so called Auger electron originates from a secondary process. The kinetic energy E_kinetic of the Auger electron is given by

$$E_\mathrm{kinetic} = E_\mathrm{m} - E_\mathrm{n} - E_\mathrm{l} = h\nu_\mathrm{f} - E_\mathrm{l} \tag{2.2.16}$$

and is thus equal to the fluorescence photon reduced by the binding energy E_l [5–7].

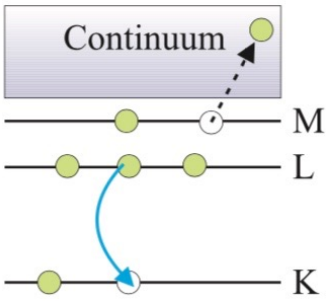

Figure 2.6: Illustration of the Auger effect. The excess energy of the transition of the electron from the L-shell to the hole in the K-shell is transferred to an electron in the M-shell, which is subsequently expelled from the atom [6].

2.2.4.4 Pair Production

In the Coulomb field of the atomic nucleus, a photon with energy larger than twice the rest mass of an electron, $h\nu > 2m_\mathrm{e}c^2$, can be converted into a pair of an electron and a positron. From the subsequent annihilation of the positron with an electron a pair of 511 keV photons is produced, emitted in opposite directions with approximately 180°.

An electron-positron pair can also be generated in the Coulomb field of an electron in the atomic shell during the so called 'triplet-production', where the condition $h\nu > 4m_\mathrm{e}c^2$ has to be fulfilled. The shell electron is expelled in this process. The probability for this effect is significantly smaller than for the pair production [7**?**].

2.2.5 Mass Attenuation Coefficient

The linear absorption coefficient μ is the sum of the interaction coefficients σ_i for interactions of type i. Dominant contributions are the photoelectric effect τ, Compton effect σ_{C}, coherent scattering σ_{coh} and the pair production κ:

$$\mu = \sum_i \sigma_i = \tau + \sigma_{\mathrm{C}} + \sigma_{\mathrm{coh}} + \kappa \tag{2.2.17}$$

The relative probability for the occurrence of the respective effect as a function of the atomic number of the absorber or of the photon energy is shown in Fig. 2.7. Contributions of other interaction mechanisms are negligible in general. The interaction coefficients are proportional to the atomic interaction cross sections and therefore show the same dependence on photon energy and atomic number of the absorber.

While traversing through an infinitesimal distance $\mathrm{d}z$ of material of density ρ, the mean fraction of the particles which interact in one of the listed ways is given by $\frac{\mathrm{d}N}{N}$. Using the Avogadro constant N_{A} and the molar mass M_{A}, the mass attenuation coefficient is given by

$$\frac{\mu}{\rho} = \frac{1}{\rho\,\mathrm{d}z}\frac{\mathrm{d}N}{N} = \frac{N_{\mathrm{A}}}{M_{\mathrm{A}}}\sum_i \sigma_i = \sum_i \left(\frac{\mu}{\rho}\right)_i \tag{2.2.18}$$

This is generally valid for uncharged particles of a given type and energy [5, 10].

Considering a beam of photons traveling through an infinitesimal sheet with thickness dz of a certain material in a depth z, interaction processes discussed before lead to an exponential decrease of the particle number $N(z)$ (Fig. 2.8). For the particle number $N(z)$ it is valid

$$-\,\mathrm{d}N = N(z)\mu\,\mathrm{d}z \tag{2.2.19}$$

which can be expressed as differential equation

$$\frac{\mathrm{d}N}{N(z)} = -\mu\,\mathrm{d}z \tag{2.2.20}$$

whose solution is found by define $N_0 = N(z=0)$ to be the initial particle number at $z = 0$:

$$N(z) = N_0 e^{-\mu z} \tag{2.2.21}$$

Since every coefficient in Equ. 2.2.17 is proportional to the absorber density ρ, the

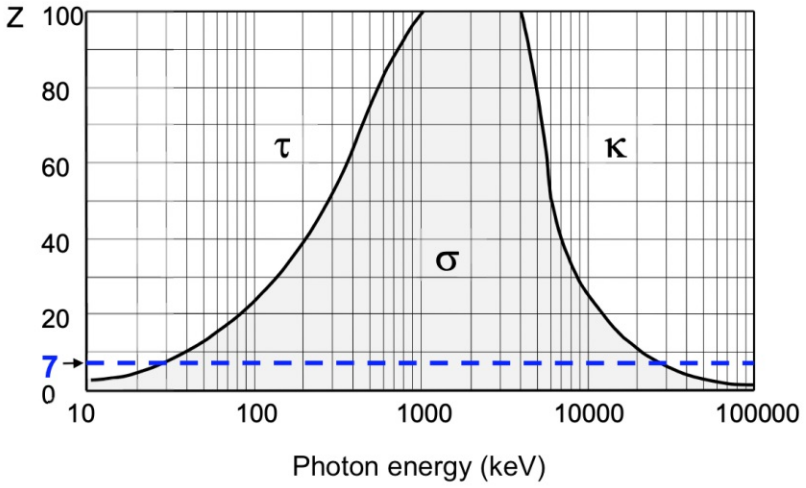

Figure 2.7: Ratios of the dominant photon interaction probabilities for the most important interaction mechanisms, the photoelectric effect τ, the Compton effect σ and the pair production κ, in dependence of the nuclear charge number Z of the absorber and the photon energy. $Z = 7$ corresponds to the typical mean nuclear charge number of tissues, water and phantom materials. Along the lines delimiting the areas, the respective probabilities are equal [5].

mass attenuation coefficient μ/ρ is considered in most cases (Fig. 2.9). Equ. 2.2.21 then transforms to

$$N(z) = N_0 e^{-\frac{\mu}{\rho}\rho z} \tag{2.2.22}$$

with the area density ρz [5–7].

2.2.6 Mass Energy-Transfer Coefficient

For uncharged particles of a given type and radiant energy R the mass energy-transfer coefficient $\frac{\mu_{\mathrm{tr}}}{\rho}$ is given by

$$\frac{\mu_{\mathrm{tr}}}{\rho} = \frac{1}{\rho\,\mathrm{d}z}\frac{\mathrm{d}R_{\mathrm{tr}}}{R} = \frac{N_{\mathrm{A}}}{M_{\mathrm{A}}}\sum_i f_i\sigma_i \tag{2.2.23}$$

where ρ is the density of the material, and $\mathrm{d}R_{\mathrm{tr}}$ is the kinetic energy transferred to charged particles during interaction processes of the incident particles traversing a distance of dz through the material. f_i is the ratio of kinetic energy transferred to charged particles during an interaction of type i to the kinetic energy of the incident uncharged particle [10]. The mass energy-transfer coefficient thus determines the total initial kinetic energy of all electrons which are released or produced dur-

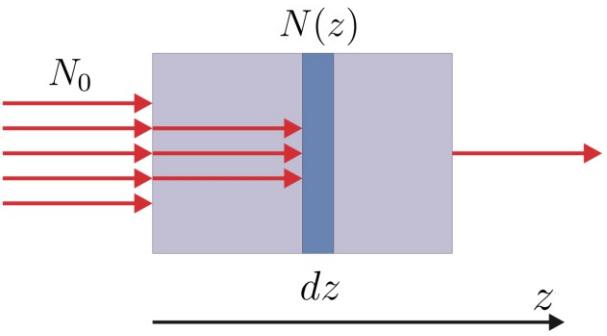

Figure 2.8: Attenuation of a narrow beam traveling through material in the specified direction z [6].

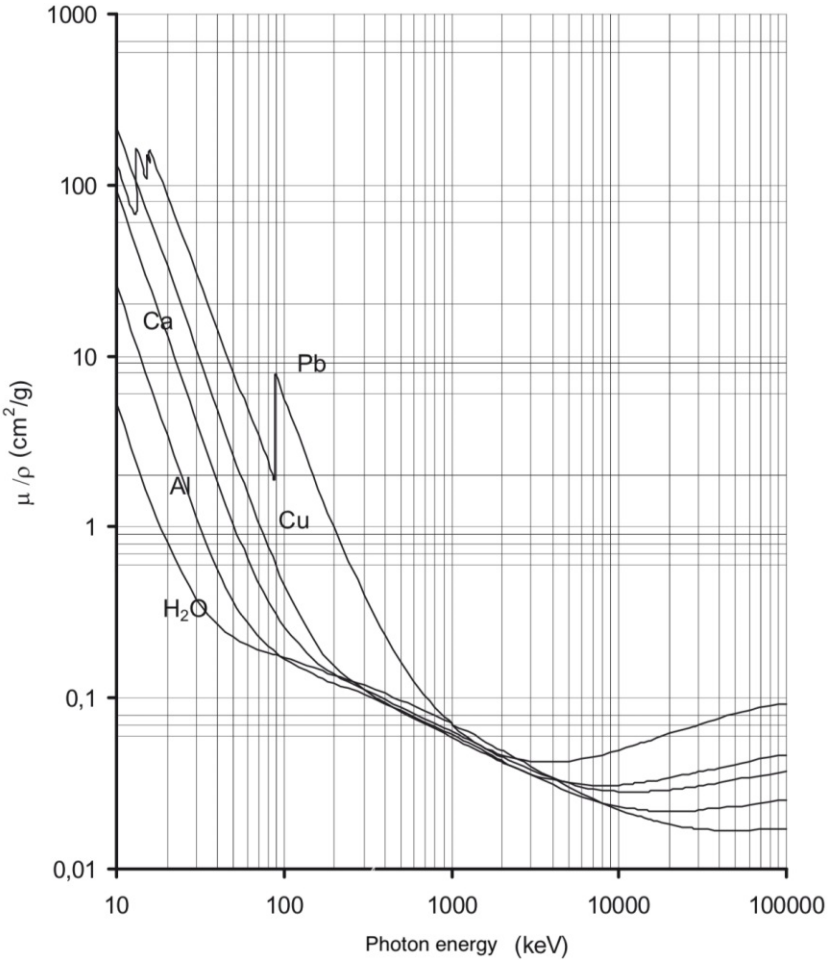

Figure 2.9: Mass attenuation coefficients for various materials [5].

ing direct interaction of the photons (photoelectric effect, Compton effect and pair production) as well as electrons emitted indirectly (Auger effect).

In simple terms, the linear energy-transfer coefficient for a given photon energy E can be calculated by multiplying the linear absorption coefficient μ by the relative energy transfer $\overline{E}_{\mathrm{tr}}/E$ to charged secondary particles averaged over all interactions involved:

$$\mu_{\mathrm{tr}} = \frac{\overline{E}_{\mathrm{tr}}}{E} \cdot \mu \tag{2.2.24}$$

Analogous to the linear absorption coefficient, the linear energy-transfer coefficient is given as a sum of coefficients $\mu_{\mathrm{tr,i}}$ for each interaction process:

$$\mu_{\mathrm{tr}} = \mu_{\mathrm{tr},\tau} + \mu_{\mathrm{tr},\sigma_{\mathrm{C}}} + \mu_{\mathrm{tr},\kappa} \tag{2.2.25}$$

where the photoelectric effect (τ), the Compton effect (σ_{C}) and the pair production (κ) are assumed to contribute dominantly. Triplet production is negligible and coherent scattering does not contribute to energy transfer. Material and energy-dependent transfer factors t_i can be applied on the interaction coefficients for the corresponding interaction mechanism as weighting factors

$$\mu_{\mathrm{tr}} = t_\tau \cdot \tau + t_{\mathrm{C}} \cdot \sigma_{\mathrm{C}} + t_\kappa \cdot \kappa \tag{2.2.26}$$

which allows the calculation of each partial coefficient in Equ. 2.2.25 [5, 7].

2.2.7 Mass Energy-Absorption Coefficient

Charged particles set free by uncharged particles incident on a material slow to rest due to interaction processes whereby an average material-specific fraction g of the kinetic energy is converted to photon radiation due to radiative processes. These include bremstrahlung generation, annihilation processes and fluorescence. The mass energy-transfer coefficient reduced by this radiative fraction by multiplying with $(1-g)$ is the mass energy-absorption coefficient:

$$\frac{\mu_{\mathrm{en}}}{\rho} = \frac{\mu_{\mathrm{tr}}}{\rho} \cdot (1-g) \tag{2.2.27}$$

The mass energy-absorption coefficient thus indicates the energy absorbed locally in the material at the point of interaction [5, 10].

2.3 Physical Dose Quantities

Among others, two physical dose quantities, absorbed dose and kerma, were of importance in this work and are presented in the following.

2.3.1 Absorbed Dose

Absorbed dose D_{mat} is the mean energy $d\bar{\epsilon}$ locally absorbed in a volume element $\mathrm{d}V$ with mass $\mathrm{d}m$ and density ρ_{mat} of an absorber material during an irradiation (Fig. 2.10 left):

$$D_{\mathrm{mat}} = \frac{\mathrm{d}\bar{\epsilon}}{\mathrm{d}m} = \frac{1}{\rho_{\mathrm{mat}}} \cdot \frac{\mathrm{d}\bar{\epsilon}}{\mathrm{d}V} \tag{2.3.1}$$

$\mathrm{d}\bar{\epsilon}$ results from energy deposits ϵ_i during single interactions i. Thus, the energy $\bar{\epsilon}$ deposited in a certain volume of matter is given by

$$\bar{\epsilon} = \sum_i \epsilon_i \tag{2.3.2}$$

Considering an incident particle with energy ϵ_{in} (excluding the rest energy) undergoing an interaction in the mass volume considered, the energy balance is given by

$$\epsilon_i = \epsilon_{\mathrm{in}} - \epsilon_{\mathrm{out}} + Q \tag{2.3.3}$$

where the deposition energy ϵ_i is reduced by the sum of energies (excluding rest energy) of all ionizing particles leaving the volume dV. Q indicates changes in the rest energies of the nucleus and of all particles involved (decrease for $Q > 0$, increase for $Q < 0$).

Secondary electrons carry the major part of absorbed dose, whereby the ionization energies are characteristic for every material, which is why the absorber material always has to be specified. SI-unit of the absorbed dose is 1 Gray (Gy), whereby 1 Gy = 1 J kg^{-1} [2, 10, 11].

2.3.2 Kerma

Kerma K_{mat} is the sum of the initial kinetic energies $\mathrm{d}E_{\mathrm{tr}}$ of charged secondary particles released in a certain material with density ρ_{mat} by indirectly ionizing radiation per unit mass $\mathrm{d}m$ in a volume element $\mathrm{d}V$ considered (Fig. 2.10 right):

$$K_{\mathrm{mat}} = \frac{\mathrm{d}E_{\mathrm{tr}}}{\mathrm{d}m} = \frac{1}{\rho_{\mathrm{mat}}} \cdot \frac{\mathrm{d}E_{\mathrm{tr}}}{\mathrm{d}V} \tag{2.3.4}$$

$\mathrm{d}E_{\mathrm{tr}}$ includes kinetic energy of charged particles emitted in course of radioactive transitions of excited atoms or molecules or nuclear processes.

Kerma is an abbreviation for 'kinetic energy released per unit mass'. Just like absorbed dose, Kerma is strongly determined by ionization energies of the regarding material and which has to be specified. For instance, the air kerma K_{a} corresponds to the kerma in dry air at reference conditions which are specified as a temperature of 20°C and pressure of 101,33 kPa [10]. SI-unit of the kerma is 1 Gray (Gy), whereby 1 Gy = 1 J kg^{-1}. [10, 11].

In the following discussion, we omit the index 'mat' for clarity. For a given fluence Φ of uncharged particles with energy E, the kerma K for a certain material is given by

$$K = \Phi \cdot E \cdot \frac{\mu_{\mathrm{tr}}}{\rho} \tag{2.3.5}$$

The mass energy-transfer coefficient μ_{tr}/ρ was already discussed before. In general, the particle fluence will show a spectral distribution with respect to the energy E, represented by $\Phi_E = \frac{\mathrm{d}\Phi}{\mathrm{d}E}$. In integral notation, the kerma can be written as

$$K = \int \Phi_E \cdot E \cdot \frac{\mu_{\mathrm{tr}}}{\rho}\, \mathrm{d}E \tag{2.3.6}$$

For special circumstances, the kerma can be used as an approximation to absorbed dose. Considering the existence of charged-particle equilibrium as well as negligibility of radiative losses, and as an additional requirement that the binding energy of the liberated charged particles is small compared to the kinetic energy of the uncharged particles, the numerical value of the kerma approaches to that of absorbed dose.

The collision kerma K_{col} is related to the kerma and has long been used as an approximation for the absorbed dose in case that radiative losses are not negligible and is defined as

$$K_{\mathrm{col}} = E \cdot \Phi \cdot \frac{\mu_{\mathrm{en}}}{\rho} = E \cdot \Phi \cdot \frac{\mu_{\mathrm{tr}}}{\rho} \cdot (1-g) = K \cdot (1-g) \tag{2.3.7}$$

The collision kerma is expressed in integral notation is given as

$$K_{\mathrm{col}} = \int \Phi_E \cdot E \cdot \frac{\mu_{\mathrm{en}}}{\rho}\, \mathrm{d}E = \int \Phi_E \cdot E \cdot \frac{\mu_{\mathrm{tr}}}{\rho} \cdot (1-g)\, \mathrm{d}E = K \cdot (1-\bar{g}) \tag{2.3.8}$$

resulting in a mean value $\bar{g}$ for the radiative energy loss [10].

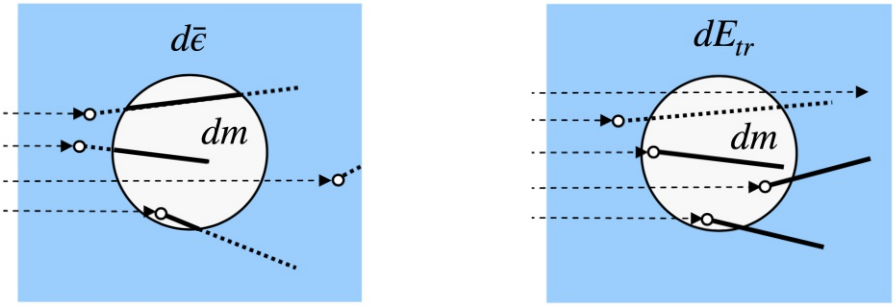

Figure 2.10: Illustration on the definition of absorbed dose (left) and kerma (right). Small circles represent points were an electron is liberated. Dotted lines represent energy transfer not counting to absorbed dose or kerma, energy transfer represented by bold lines contribute since charge carriers are liberated on their path due to ionization processes [11].

2.4 Protection Quantities

Stochastic risks like cancer induction or hereditary damage in connection with exposure of a person to ionizing radiation are derived by usage of the concept of protection quantities. Therewith exposure limits can be specified to ensure that the risk of occurrence of stochastic health effects is kept below acceptable levels.

'Protection quantity' is a collective term for tissue equivalent doses H_{T} and effective dose E which are not measurable per definition since H_{T} is averaged over organs and E is a risk-weighted quantity for the estimation of the exposure-risk. The basis for the definition of the protection quantities is the absorbed dose $D_{\mathrm{T,R}}$ averaged over the volume of a certain organ (or tissue) for radiation of the type R with an associated radiation weighting factor w_{R}. w_{R} implies the biological effectiveness for the regarding radiation quality (Tab. 2.1). Accordingly, the tissue equivalent dose H_{T} in an organ or in tissue is defined by

$$H_{\mathrm{T}} = \sum_{\mathrm{R}} w_{\mathrm{R}} D_{\mathrm{T,R}} \tag{2.4.1}$$

SI-unit of the equivalent dose is 1 Sievert (Sv), whereby 1 Sv = 1 J kg^{-1}.

Based on the equivalent dose in an organ or tissue, the effective dose E is defined by the sum of tissue equivalent doses, weighted by the sensitivity of each organ to the induction of stochastic effects by assigning corresponding tissue weighting factors w_{T} (Tab. 2.2). For all tissues T assumed to be sensitive to induce stochastic effects due to ionizing radiation, it holds $\sum_{\mathrm{T}} w_{\mathrm{T}} = 1$. The effective dose E therefore is

defined by

$$E = \sum_{\mathrm{T}} w_{\mathrm{T}} H_{\mathrm{T}} = \sum_{\mathrm{T,R}} w_{\mathrm{T}} w_{\mathrm{R}} D_{\mathrm{T,R}} \tag{2.4.2}$$

SI-unit of the effective dose is 1 Sievert (Sv), whereby 1 Sv = 1 J kg^{-1} [2, 11, 12].

Radiation type R	Radiation weighting factor w_{R}
Photons	1
Electrons, muons	1
Protons, charged pions	2
Alpha-particles, fission fragments, heavy ions	20
Neutrons	continuous function of neutron energy

Table 2.1: Radiation weighting factors for various particles [12].

Tissue T	Tissue weighting factor w_{T}
Gonads	0,08
Colon	0,12
Lung	0,12
Stomach	0,12
Red Bone Marrow	0,12
Breast	0,12
Sum of remaining tissues	0,12
Bladder	0,04
Oesophagus	0,04
Liver	0,04
Thyroid	0,04
Bone surface	0,01
Brain	0,01
Salivary glands	0,01
Skin	0,01

Table 2.2: Radiation weighting factors w_{T} for various particles [12].

2.5 Operational Quantities According to ICRU Report 39/51

The concepts of operational dose quantities valid so far were proposed in ICRU Report 39/51 [3, 4] and represent the measurands currently in use in practical radiation protection.

2.5.1 Definitions

To obtain an assessment of the effective dose, which is not measurable by its nature, operational dose quantities were introduced. These are based on the dose equivalent H which is the product

$$H = Q \cdot D \tag{2.5.1}$$

at a point in a material or tissue considered, with Q being the quality factor and D the absorbed dose. Q specifies the biological effectiveness for the regarding radiation quality based on the values for the linear energy transfer (LET, L_∞) in water.

A separation of quantities for the purpose of monitoring persons or for monitoring of the environment was made. The personal dose equivalent $H_\mathrm{p}(d)$ with $d = 0,07$ mm for local skin, $d = 3$ mm for the lens of the eye and d =10 mm for the whole body, represents the dose equivalent in the depth d in mm under a representative location on the body. Conversion coefficients were calculated in simple geometrical phantoms like the slab, cylinder and rod phantom, respectively. The directional dose equivalent $H'(d, \Omega)$ as well as the ambient dose equivalent $H^*(d)$ are defined in the ICRU sphere in the depth d and with radiation incidence direction Ω. The radiation field is considered to be expanded, spatially homogeneous and aligned. An overview of the operational dose quantities and their relation to the protection quantities is shown in Tab. 2.3 [11**?**].

2.5.2 Limitations

Due to their different definitions, protection quantities and operational quantities show inconsistencies in certain energy ranges. Furthermore, the definition of the quality factor $Q(L)$ and of the radiation weighting factor w_R are defined inconsistently leading to differing estimated radiation effectiveness.

As an example, the personal dose equivalent $H_\mathrm{p}(d)$ is defined in the depth d in the human body, whereas for the calculation of conversion coefficients, the simple slab, rod and pillar phantoms are used. For different locations on the body, which

	Whole body	Lens of the eye	Local skin
Protection quantites:			
	Effective dose E	Equivalent dose in the lens of the eye $H_{\mathrm{T\ lens}}$	Equivalent dose in local skin $H_{\mathrm{T\ local\ skin}}$
Operational quantities:			
Area monitoring	Ambient dose equivalent $H^*(10)$	Directional dose equivalent $H'(3, \Omega)$	Directional dose equivalent $H'(0.07, \Omega)$
Individual monitoring	Personal dose equivalent $H_{\mathrm{p}}(10)$	Personal dose equivalent $H_{\mathrm{p}}(3)$	Personal dose equivalent $H_{\mathrm{p}}(0.07)$

Table 2.3: Overview of the protection quantities and the operational quantities according to ICRU Report 39/51 [3, 4].

shows great geometrical complexity, the applicability of the tabulated conversion coefficients calculated about three decades ago must be questioned or certainly does not reflect reality. The same applies for measurements in a depth of 10 mm since organs are located at different depths. Further, the phantoms are defined to consist of ICRU 4-element tissue, which is not producible.

For photon energies below 70 keV, effective dose is significantly overestimated by $H_{\mathrm{p}}(10)$ (Fig. 2.11). In this figure, another aspect is pointed out: A common time-saving approach in simulations is use of the kerma approximation (Sec. 4.1). Here, energy deposition of a photon in tissue is located at the point of interaction, not including transport of electrons expelled from the tissue atoms due to ionization processes. In general, this is a satisfying approximation, but nevertheless, discrepancies between the values for the protection and for the operational quantities are noticeable. The calculation including electron transport leads to an underestimate of effective dose and is therefore less conservative, which is one reason why the kerma approximation was applied.

Inconsistencies are also found for the other particles, which do not play a role in this work, where we have considered only photon radiation. The poor estimations of the protection quantities for certain particles in certain energy ranges where the impetus for the redefinition of the operational quantities [2, 13].

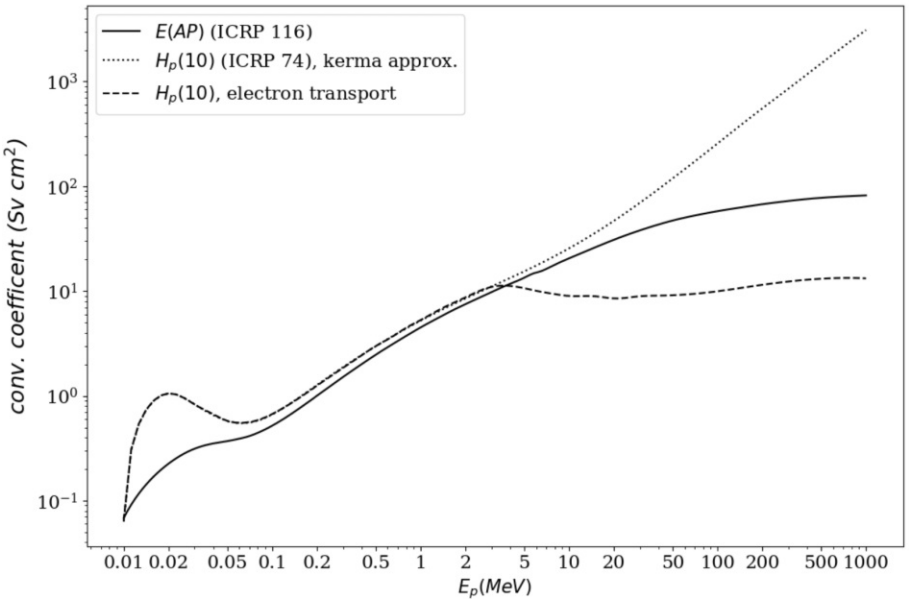

Figure 2.11: Conversion coefficients fluence to effective dose in antero-posterior irradiation (solid line), to personal dose equivalent $H_{\mathrm{p}}(10, 0°)$ calculated in kerma approximation (dotted line) and to personal dose equivalent calculated with full electron transport (dashed line) [13].

2.6 Recommended New Operational Quantities for External Radiation Exposure

2.6.1 Fundamentals

Operational quantities H_{R} for external exposure of radiation of type R with particle energy E_{p} are all together defined as a product of a dosimetric quantity (in the following we always use the particle fluence Φ_{R}, alternatively, air kerma can be used) and a conversion coefficient $h_{\mathrm{R}}(E_{\mathrm{p}})$:

$$H_{\mathrm{R}} = h_{\mathrm{R}}(E_{\mathrm{p}}) \cdot \Phi_{\mathrm{R}} \tag{2.6.1}$$

The analogy to the definition of the protection quantities is immediately apparent. A more general expression including multidirectional radiation incidence (direction Ω) and energy distributions results from the integration

$$H_{\mathrm{R}}(\Omega) = \int h_{\mathrm{R}}(E_{\mathrm{p}}, \Omega) \cdot \Phi_{\mathrm{R}}(E_{\mathrm{p}}, \Omega)\, \mathrm{d}E_{\mathrm{p}} \tag{2.6.2}$$

	Whole body	Lens of the eye	Local skin
Protection quantites:			
	Effective dose E	Equivalent dose in the lens of the eye $H_{\mathrm{T\ lens}}$	Equivalent dose in local skin $H_{\mathrm{T\ local\ skin}}$
Operational quantities:			
Area monitoring	Ambient dose H^*	Directional absorbed dose in the lens of the eye $D'_{\mathrm{lens}}(\Omega)$	Directional absorbed dose in local skin $D'_{\mathrm{local\ skin}}(\Omega)$
Individual monitoring	Personal dose H_{p}	Personal absorbed dose in the lens of the eye $D_{\mathrm{p\ lens}}$	Personal absorbed dose in local skin $D_{\mathrm{p\ local\ skin}}$

Table 2.4: Overview of the protection quantities and the recommended operational quantities.

The conversion coefficient is therefore given by

$$h_{\mathrm{R}}(E_{\mathrm{p}}, \Omega) = \frac{H_{\mathrm{R}}(E_{\mathrm{p}}, \Omega)}{\Phi_{\mathrm{R}}(E_{\mathrm{p}}, \Omega)} \tag{2.6.3}$$

Here, $H_{\mathrm{R}}(E_{\mathrm{p}}, \Omega)$ is calculated on the corresponding phantom and $\Phi_{\mathrm{R}}(E_{\mathrm{p}}, \Omega)$ is the particle fluence in absence of the phantom. Due to the strong similarities of the recommended operational quantities to the protection quantities they are now better approximated and are even numerically identical for certain particle energies and radiation incidence directions [2].

2.6.2 Ambient Dose

At an arbitrary point in a radiation field, the ambient dose H^* is the product of the particle fluence Φ at this point and a conversion coefficient h^* which links the particle fluence to the maximum value E_{max} of effective dose. The conversion coefficient $h^*_i(E_{\mathrm{p}})$ for particles of type i with kinetic energy E_{p} is given by

$$h^*_i(E_{\mathrm{p}}) = \frac{E_{\mathrm{max},i}(E_{\mathrm{p}})}{\Phi_i(E_{\mathrm{p}})} \tag{2.6.4}$$

and is calculated for the whole-body ICRP/ICRU adult reference phantom in an expanded and aligned radiation field. In case of an energy distribution of particles

of type i it is to integrate

$$H_i^* = \int h_i^*(E_\mathrm{p}) \left[\frac{\mathrm{d}\Phi_i(E_\mathrm{p})}{\mathrm{d}E_\mathrm{p}} \right] \mathrm{d}E_\mathrm{p} \tag{2.6.5}$$

and the contributions of different particles types are summed

$$H^* = \sum_i H_i^* \tag{2.6.6}$$

Coherent SI-unit of the ambient dose is J kg^{-1} with the special name Sievert (Sv) [2].

2.6.3 Directional Absorbed Dose in the Lens of the Eye

At an arbitrary point in a radiation field with direction of incidence Ω, the directional absorbed dose in the lens of the eye $D'_\mathrm{lens}(\Omega)$ is the product of the particle fluence $\Phi(\Omega)$ at this point and a conversion coefficient $d'_\mathrm{lens}(\Omega)$ which links the particle fluence to the maximum value of the absorbed dose in the lens of the left or right eye. The conversion coefficient $d'_{\mathrm{lens},i}(E_\mathrm{p}, \Omega)$ for particles of type i with kinetic energy E_p is given by

$$d'_{\mathrm{lens},i}(E_\mathrm{p}, \Omega) = \frac{D'_{\mathrm{lens},i}(E_\mathrm{p}, \Omega)}{\Phi_i(E_\mathrm{p}, \Omega)} \tag{2.6.7}$$

and is calculated for the eye model embedded in the whole body-phantom [14] in an expanded and aligned radiation field incident from direction Ω. In case of an energy distribution of particles of type i it is to integrate

$$D'_{\mathrm{lens},i}(\Omega) = \int d'_{\mathrm{lens},i}(E_\mathrm{p}, \Omega) \left[\frac{\mathrm{d}\Phi_i(E_\mathrm{p}, \Omega)}{\mathrm{d}E_\mathrm{p}} \right] \mathrm{d}E_\mathrm{p} \tag{2.6.8}$$

and the contributions of different particles types incident from direction Ω are summed

$$D'_\mathrm{lens}(\Omega) = \sum_i D'_{\mathrm{lens},i}(\Omega) \tag{2.6.9}$$

Coherent SI-unit of the directional absorbed dose in the lens of the eye is J kg^{-1} with the special name Gray (Gy) [2].

2.6.4 Directional Absorbed Dose in Local Skin

At an arbitrary point in a radiation field with direction of incidence Ω, the directional absorbed dose in local skin $D'_{\mathrm{local\ skin}}(\Omega)$ is the product of the particle fluence $\Phi(\Omega)$ at

this point and a conversion coefficient $d'_{\text{local skin}}(\Omega)$ which links the particle fluence to the value of absorbed dose in local skin. The conversion coefficient $d'_{\text{local skin},i}(E_\text{p}, \Omega)$ for particles of type i with kinetic energy E_p is given by

$$d'_{\text{local skin},i}(E_\text{p}, \Omega) = \frac{D'_{\text{local skin},i}(E_\text{p}, \Omega)}{\Phi_i(E_\text{p}, \Omega)} \tag{2.6.10}$$

and is calculated for an ICRU 4-element tissue phantom slab with the dimensions 300 mm × 300 mm × 148 mm (density of 1,0 g cm^{-3}) whose front surface is covered with 2 mm skin (density of 1,09 g cm^{-3}) [15, 16] in an expanded and aligned radiation field incident from direction Ω. In case of an energy distribution of particles of type i it is integrated

$$D'_{\text{local skin},i}(\Omega) = \int d'_{\text{local skin},i}(E_\text{p}, \Omega) \left[\frac{\mathrm{d}\,\Phi_i(E_\text{p}, \Omega)}{\mathrm{d}E_\text{p}}\right] \mathrm{d}E_\text{p} \tag{2.6.11}$$

and the contributions of different particles types incident from direction Ω are summed

$$D'_{\text{local skin}}(\Omega) = \sum_i D'_{\text{local skin},i}(\Omega) \tag{2.6.12}$$

Coherent SI-unit of the directional absorbed dose in local skin is J kg^{-1} with the special name Gray (Gy) [2].

2.6.5 Personal Dose

The personal dose H_p is the product of the particle fluence Φ at a point on the human body and a conversion coefficient h_p which links the particle fluence to the value of effective dose E. The conversion coefficient $h_{\text{p},i}(E_\text{p}, \Omega)$ for particles of type i with kinetic energy E_p incident from direction Ω is given by

$$h_{\text{p},i}(E_\text{p}, \Omega) = \frac{E_i(E_\text{p}, \Omega)}{\Phi_i(E_\text{p}, \Omega)} \tag{2.6.13}$$

and is calculated on the ICRU adult reference phantoms [15], which is also used for the calculation of conversion coefficients relating to the protection quantities, for broad parallel beams in vacuum for a set of angles φ (0° to 90° in 15° steps ad for 180°). For a distribution of kinetic energies E_p in the interval $\mathrm{d}E_\text{p}$ and directions of incidence Ω in the interval $\mathrm{d}\Omega$, it is integrated

$$H_{\text{p},i} = \int\int h_{\text{p},i}(E_\text{p}, \Omega) \cdot \left[\frac{\mathrm{d}^2\,\Phi_i(E_\text{p}, \Omega)}{\mathrm{d}E_\text{p}\mathrm{d}\Omega}\right] \mathrm{d}E_\text{p} d\Omega \tag{2.6.14}$$

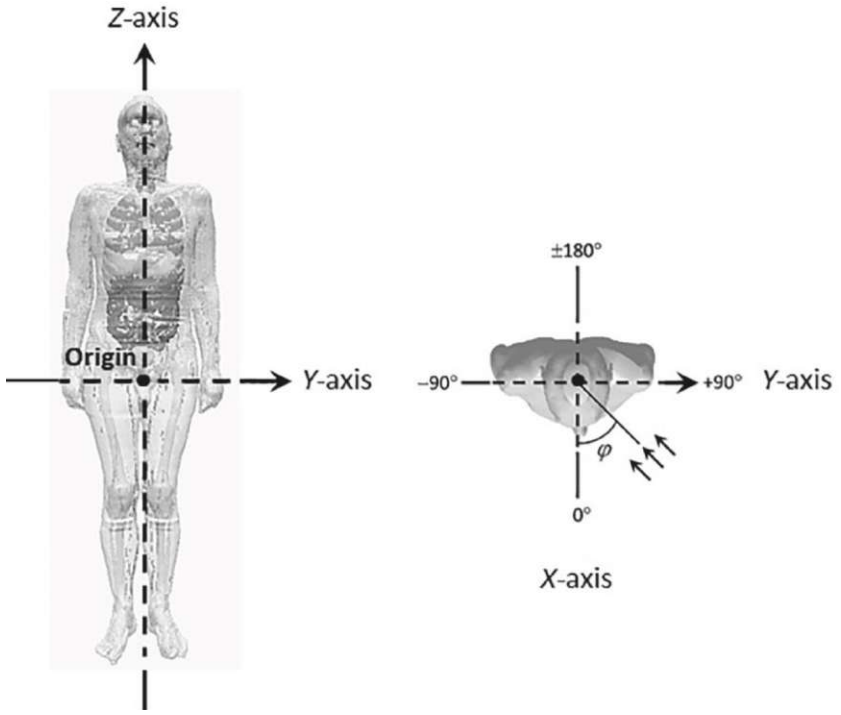

Figure 2.12: Orientation of the coordinate system used for the definition of the personal dose H_p [2]

and the contributions of different particle types are summed

$$H_\mathrm{p} = \sum_i H_{\mathrm{p},i} \tag{2.6.15}$$

Coherent SI-unit of the personal dose is J kg^{-1} with the special name Sievert (Sv).

The coordinate system is defined with its origin in the midpoint of the body (Fig. 2.12). The x-axis runs from the back to the front, the y-axis runs from the right to the left from the point of view from the body, and the z-axis is from toe to head. Ω, the irradiation directional angle, consists of the two components θ, the angle with respect to the z-axis, and φ, the angle with respect to the x-axis in the xy-plane [2].

By definition, the numerical values of conversion coefficients from radiometric or dosimetric quantities to personal dose and conversion coefficients to effective dose are equal at certain particle energies and irradiation direction angles [2].

2.6.6 Personal Absorbed Dose in the Lens of the Eye

At an point on the head or on the body, the personal absorbed dose in the lens of the eye $D_{\mathrm{p\ lens}}$ is the product of the particle fluence Φ at this point and a conversion coefficient $d_{\mathrm{p\ lens}}$ which links the particle fluence to the maximum value of absorbed dose in the lens of the left or right eye. The same coordinate system as for the personal dose H_{p} is used. The conversion coefficient $d_{\mathrm{p\ lens},i}(E_{\mathrm{p}}, \Omega)$ for particles of type i with kinetic energy E_{p} incident from direction Ω is given by

$$d_{\mathrm{p\ lens},i}(E_{\mathrm{p}}, \Omega) = \frac{D_{\mathrm{p\ lens},i}(E_{\mathrm{p}}, \Omega)}{\Phi_i(E_{\mathrm{p}}, \Omega)} \tag{2.6.16}$$

and is calculated for the eye model embedded in the whole body-phantom [14] in an expanded and aligned radiation field incident from direction Ω. In case of an energy distribution of particles of type i it is to integrate

$$D_{\mathrm{p\ lens},i} = \int\int d_{\mathrm{p\ lens},i}(E_{\mathrm{p}}, \Omega) \left[\frac{\mathrm{d}^2\Phi_i(E_{\mathrm{p}}, \Omega)}{\mathrm{d}E_{\mathrm{p}}\mathrm{d}\Omega}\right] \mathrm{d}E_{\mathrm{p}}\mathrm{d}\Omega \tag{2.6.17}$$

and the contributions of different particles types incident from direction Ω are summed

$$D_{\mathrm{p\ lens}} = \sum_i D_{\mathrm{p\ lens},i} \tag{2.6.18}$$

Coherent SI-unit of the personal absorbed dose in the lens of the eye is J kg^{-1} with the special name Gray (Gy) [2].

2.6.7 Personal Absorbed Dose in Local Skin

At an point on the body or on extremities in a radiation field, the personal absorbed dose in local skin $D_{\mathrm{p\ local\ skin}}$ is the product of the particle fluence Φ at this point and a conversion coefficient $d'_{\mathrm{p\ local\ skin}}$ which links the particle fluence to the value of absorbed dose in local skin. The same coordinate system as for the personal dose H_{p} is used. The conversion coefficient $d_{\mathrm{p\ local\ skin,i}}(E_{\mathrm{p}}, \Omega)$ for particles of type i with kinetic energy E_{p} incident from direction Ω is given by

$$d_{\mathrm{p\ local\ skin},i}(E_{\mathrm{p}}, \Omega) = \frac{D_{\mathrm{\ local\ skin},i}(E_{\mathrm{p}}, \Omega)}{\Phi_i(E_{\mathrm{p}}, \Omega)} \tag{2.6.19}$$

and is calculated for ICRU slab, pillar or rod phantom [16]. In case of an energy distribution of particles of type i it is integrated

$$D_{\text{p local skin},i} = \int\int d_{\text{p local skin},i}(E_{\text{p}}, \Omega) \left[\frac{\mathrm{d}^2\Phi_i(E_{\text{p}}, \Omega)}{\mathrm{d}E_{\text{p}}\mathrm{d}\Omega}\right] \mathrm{d}E_{\text{p}}\mathrm{d}\Omega \tag{2.6.20}$$

and the contributions of different particles types incident from direction Ω are summed

$$D_{\text{p local skin}} = \sum_i D_{\text{p local skin},i} \tag{2.6.21}$$

Coherent SI-unit of the personal absorbed dose in local skin is J kg^{-1} with the special name Gray (Gy) [2].

2.7 Monte Carlo Simulations

2.7.1 Monte Carlo Method

The Monte Carlo (MC) method is a stochastic method for the determination of the time propagation of a system or model based on a sequence of random numbers. Since this sequence of random numbers is generated numerically, the term pseudo-random numbers is more appropriate. A well-conditioned random number generator produces as uniformly distributed and non-correlated numbers as possible to a degree sufficient for simulations. As an example, the MCNP6.2 RAND random number generator provides a L'Ecuyer 63-bit generator with a period of $9,2 \cdot 10^{18}$ numbers.

Particle transport, to remain in the context of this work, is not calculated by solving corresponding Boltzmann transport equation of motion for the average particle behavior, that is the essence of a deterministic method. MC simulates single particles resulting in individual tracks with uniquely assignable interactions wich are then composed to derive statements about the average behavior of a huge number of simulated particles which corresponds to a numerical experiment. Transport data including interaction cross sections and physical rules determine probability distributions which are sampled randomly.

There is a statistical uncertainty for MC simulations, which is often also referred to, albeit imprecisely, as 'statistical error' which, in general, decreases with an $\propto \frac{1}{N}$ dependence on the particle number N. This circumstance is based on the central limit theorem [17, 18].

2.7.2 Central Limit Theorem

A MC simulation determined to calculate a mean value $\overline{x}$ representing a physical quantity by sampling particle histories is assumed with N being the number of particle histories from their source generation to their death. The central limit theorem states that for N approaching to infinity the distribution function of the calculated mean x will be gaussian with a known standard deviation of $\frac{\sigma}{\sqrt{N}}$. Since σ is not known in practice, the standard deviation S is estimated, whereby this estimation is only sufficiently accurate when N is large enough to quasi-approaching infinity. In other words, repeating a simulation with N particle histories a large number of times results in a gaussian variation of the mean $\overline{x}$ with standard deviation S about the true mean [18].

Chapter 3

Materials and Experimental Methods

3.1 X-Ray unit and Spectra

The most important characteristics of the X-ray system are listed below.

- Generator: Philips MG 320 (14 kV to 320 kV tube potential)
- Tube: Philips MCN 321, 2,5 mm Be inherent filtration
- Anode: Tungsten, 40° target angle

Among others, the narrow-spectrum series (N-series) produced by this device used in the measurements meet the specifications according to ISO 4037-1 [19]. In Fig. 3.1 and Fig. 3.2, the air kerma spectra and fluence spectra of the N-series in five meters distance from the focus corresponding to the measurement setups discussed in the following are shown. Characteristics of the used spectra and calculated mean energies are listed in Tab. 3.1.

Considering a certain spectrum, the mean energy $\overline{E}_{K_\mathrm{a}}$ with regard to the air kerma is given by

$$\overline{E}_{K_\mathrm{a}} = \frac{\int K_{\mathrm{a},E} \cdot E \,\mathrm{d}E}{\int K_{\mathrm{a},E} \,\mathrm{d}E} \tag{3.1.1}$$

with the spectral air kerma $K_{\mathrm{a},E}$ for photon energy E

$$K_{\mathrm{a},E} = \Phi_E \cdot E \cdot \frac{1}{1 - g_{\mathrm{a},E}} \cdot \left(\frac{\mu_\mathrm{en}}{\rho}\right)_{\mathrm{a},E} \tag{3.1.2}$$

Φ_E is the photon fluence with respect to the photon energy E and is given by $\frac{\mathrm{d}\Phi}{\mathrm{d}E}$, where Φ is the total photon fluence. $g_{\mathrm{a},E}$ is the bremsstrahlung yield in air and

$\left(\frac{\mu_{\mathrm{en}}}{\rho}\right)_{\mathrm{a},E}$ is the spectral mass energy-absorption coefficient in air. By measurements, the number of photons with discrete energy E_i were determined [20]. The continuous integrals in Equ. 3.1.1 are then written as sums

$$\overline{E}_{K_{\mathrm{a}}} = \frac{\sum_i N_{E_i} \cdot E_i^2 \cdot \frac{1}{1-g_{\mathrm{a},E_i}} \cdot \left(\frac{\mu_{\mathrm{en}}}{\rho}\right)_{\mathrm{a},E_i}}{\sum_i N_{E_i} \cdot E_{\mathrm{i}} \cdot \frac{1}{1-g_{\mathrm{a},E_i}} \cdot \left(\frac{\mu_{\mathrm{en}}}{\rho}\right)_{\mathrm{a},E_i}} \tag{3.1.3}$$

Similarly, the mean energy $\overline{E}_{\Phi}$ with regard to the fluence Φ is given by

$$\overline{E}_{\Phi} = \frac{\int \Phi_E \cdot E \, \mathrm{d}E}{\int \Phi_E \, \mathrm{d}E} \tag{3.1.4}$$

with spectral fluence Φ_E, and in case of a discrete energy spectrum accordingly

$$\overline{E}_{\Phi} = \frac{\sum_i N_{E_i} \cdot E_i}{\sum_i N_{E_i}} \tag{3.1.5}$$

radiation quality	tube potential (kV)	$\overline{E}_{K_{\mathrm{a}}}$ (keV)	$\overline{E}_{\Phi}$ (keV)	Additional filtration thickness in mm Sn	mm Cu	mm Al
N-30	30	23,7	24,4			4,03
N-40	40	32,3	33,1			4,02
N-60	60	46,5	47,6		0,21	4,02
N-80	80	64,4	64,5		0,51	4,03
N-100	100	83,1	82,5		1,97	4,02
N-120	120	100,8	99,7	0,99	4,94	4,03
N-150	150	120,6	118,1	1,98	4,94	4,02

Table 3.1: Characteristics of the narrow-spectrum series (N-series) used in the measurements [20].

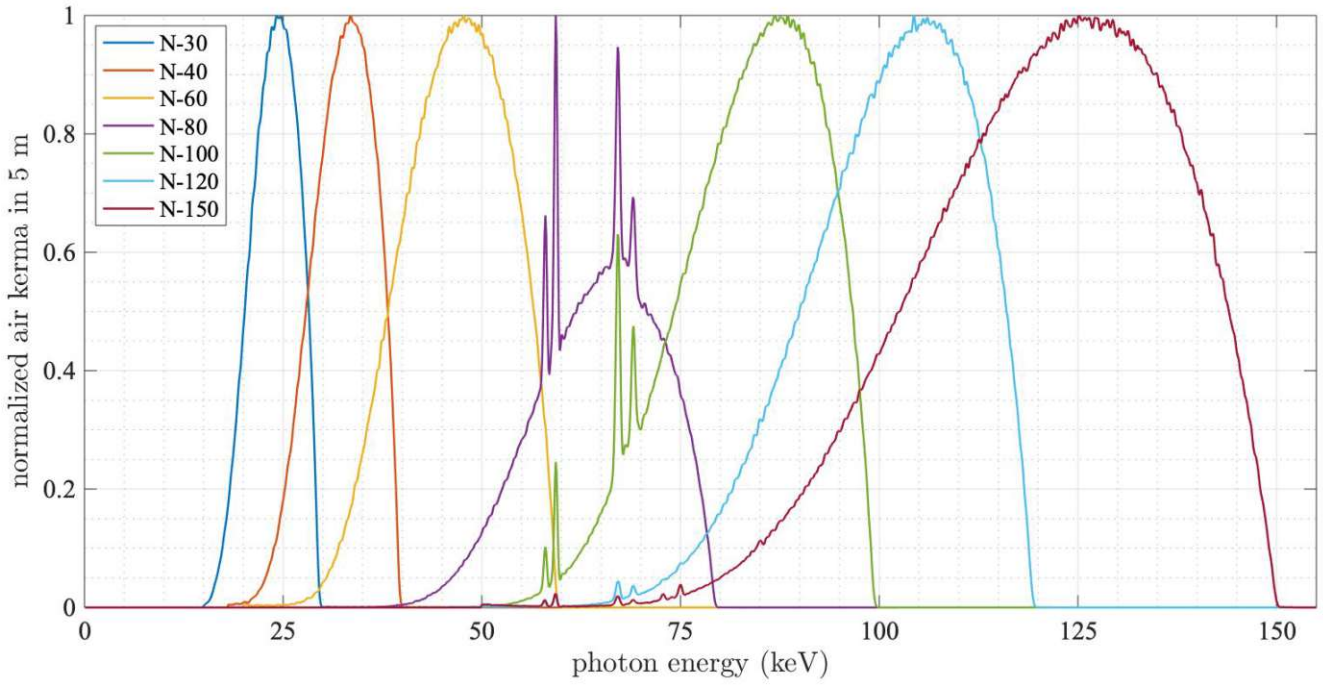

Figure 3.1: Air kerma spectra of the N-series in five meters distance from the focus [20].

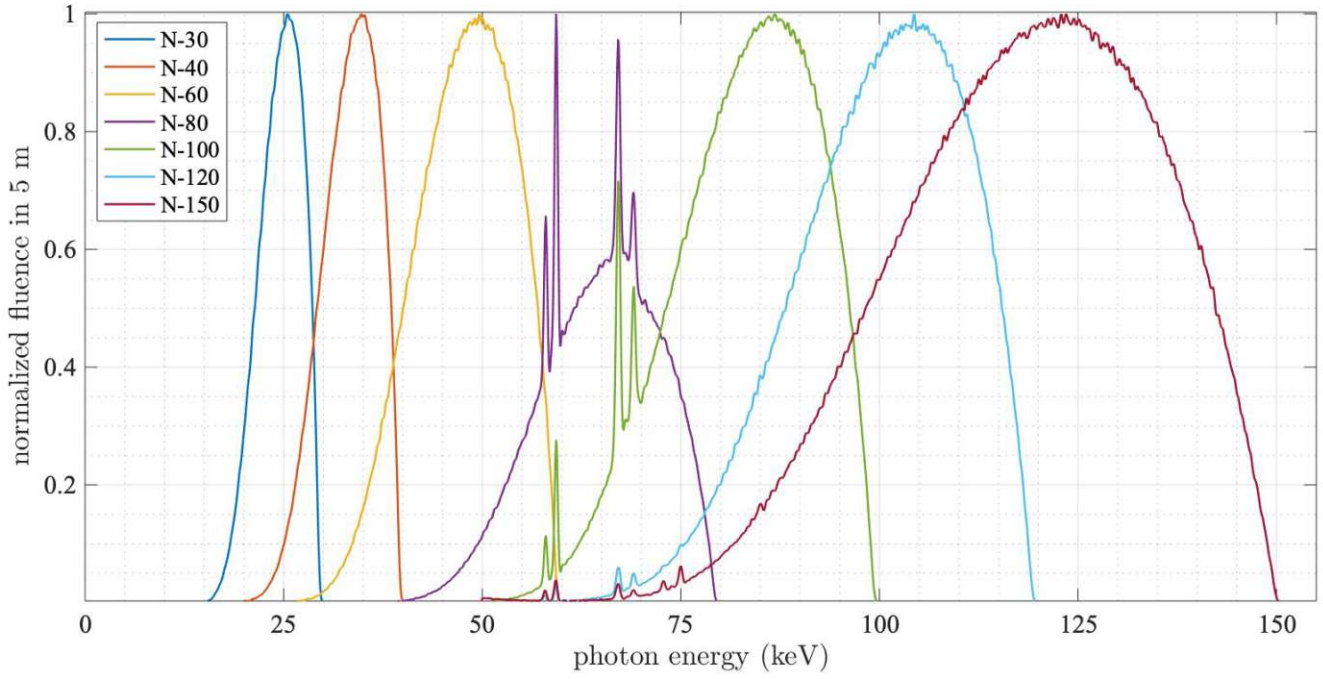

Figure 3.2: Fluence spectra of the N-series in five meters distance from the focus [20].

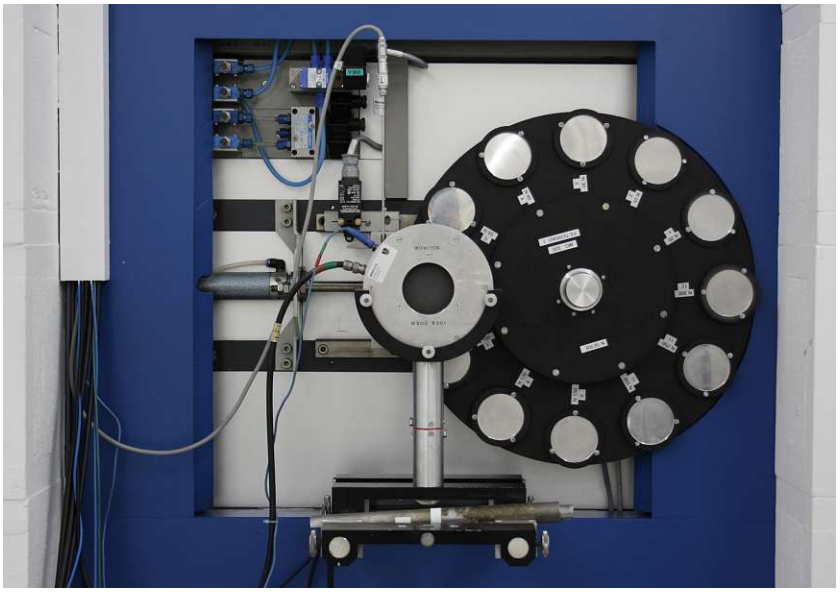

Figure 3.3: Monitor M50E-8301 in front of the filter wheel. The X-ray unit is located in the room behind the wall and can not be seen from this view.

3.2 Detectors

3.2.1 Monitor Chamber

- Manufacturer: Austrian Research Centers GmbH
- Model: M50E
- Serial number: 8301

This transmission ionization chamber was used to monitor the dose rate during the measurements to subsequently cancel out possible fluctuations. This was done by normalizing the ionization current I_C measured with an ionization chamber to the ionization current I_M of the monitor (formation of the ratio $\frac{I_C}{I_M}$). Traceability to the Austrian primary air kerma standard, which is located in same laboratory, was provided. The chamber center was located in a distance of 325 mm from the focus.

3.2.2 Shadow-Free Diagnostic Ionization Chamber (SFD)

The most important characteristics of the SFD are listed below.

- Manufacturer: PTW Freiburg
- Model: SFD chamber type 34069-2,5

- Serial number: 0018

SFD is an abbreviation for 'shadow-free diagnostic' ionization chambers for diagnostic purposes positioned in front or behind a patient equivalent phantom. The type used in this work is the SFD chamber type 34069-2,5 which is mainly used in mammography. A detailed drawing of the SFD is shown in App. B.

3.2.3 Thermoluminescent Dosemeters (TLD)

Thermoluminescent whole body dosemeters for individual monitoring of $H_p(10)$ represent a passive measurement method since the measurement result is evaluated after the irradiation and dose cannot be displayed in time.

The lithium fluoride (LiF:Mg,Ti) TLD used in the measurements were evaluated by Dosimeterservice Seibersdorf (Seibersdorf Labor GmbH). Irradiations were performed in collaboration.

3.2.4 Electronic Personal Dosemeter (EPD)

- Manufacturer: Fisher Scientific Messtechnik GmbH
- Model: EPD TrueDose G
- Serial number: 43011/1222 06110785

An electronic personal dosemeter (EPD) is an active dosemeter and displays received $H_p(0,07)$ and $H_p(10)$ in time. Measurements were carried out with a Fisher Scientific EPD TrueDose Electronic Personal Dosemeter with valid gauging.

3.3 Phantoms

3.3.1 ISO Water Slab Phantom

The ISO water slab phantom with dimensions of 30 cm × 30 cm × 15 cm is a representation for the human torso for calibration purposes. The water filled PMMA (8,05 % H, 59,99 % C, 31,96 % O, density of 1,19 g cm^{-3}) box front side is 2,5 mm and the other hull sides are 10 mm thick [21]. The following sections include images of this phantom, for example Fig. 3.4.

3.3.2 Alderson Rando Phantom

The Alderson Rando phantom is mainly used for dosimetry studies purposes in radiation therapy. It is built of a natural human skeleton embedded in tissue equivalent synthetic rubber in the shape of the upper part of human body (in our case the female body). The following sections include images of this phantom, for example Fig. 3.5.

This phantom was kindly provided by the IAEA dosimetry laboratory.

3.4 Measurement of Air Kerma

Starting a calibration chain from the austrian primary air kerma standard, a parallel plate ionization chamber, the air kerma rate for a certain spectrum in five meters distance from the focus was determined. Subsequently, the monitor chamber was calibrated by determining the monitor calibration coefficient N_{M} by

$$N_{\mathrm{M}} = \frac{\dot{K}_{\mathrm{a}}}{I_{\mathrm{M}}} \tag{3.4.1}$$

with $\dot{K}_{\mathrm{a}}$ being the air kerma rate in five meters distance and I_{M} the mean ionization current of the monitor during irradiation. Therefore, the air kerma rate free-in-air at this point could subsequently be determined using the monitor. This allowed the determination of the calibration coefficient N_{SFD} of the SFD ionization chamber free-in-air,

$$N_{\mathrm{SFD}} = \frac{\dot{K}_{\mathrm{a}}}{I_{\mathrm{SFD}}} \tag{3.4.2}$$

$\dot{K}_{\mathrm{a}}$ in this case was now the value of the air kerma rate measured by the calibrated monitor and I_{SFD} the mean ionization current of the SFD chamber. The actual determination of the air kerma rate free-in-air was always done by the monitor. However, using the SFD and the calibration coefficient N_{SFD}, the air kerma rate could have been determined in an independent measurement by

$$\dot{K}_{\mathrm{a}} = N_{\mathrm{SFD}} \cdot I_{\mathrm{SFD}} \tag{3.4.3}$$

This is strictly valid for calibration conditions.

3.5 Measurement of the Backscatter Factor Using the SFD

The phantom, ISO water slab or Alderson Rando, was positioned in that way that the point on the phantom surface at which the SFD was attached had a distance of five meters from the focus. Measurement setups are shown in Fig. 3.4 and Fig. 3.5.

The reference point on the ISO slab was right in the center of the surface facing the radiation source. It was positioned parallel and as close as possible to the slab surface. Due to the plexiglass fixation of the SFD, it could not be positioned directly on the surface so a thin gap of approximately 0,5 mm between the slab and the chamber surface arose. In case of the Alderson phantom, the center of the imaginary line connecting the two screws threads intended for attachments representing female breasts was chosen to be the reference point (which will later be referred to as 'Pos0') and therefore the approach point for the SFD. The inclination of the surface at this point was adopted for the SFD (Fig. 3.6).

The measurand was air kerma. In the following, $K_{\mathrm{a}}^{\mathrm{ph}}$ represents the air kerma on-phantom at the reference position, K_{a} the air kerma free-in-air at the same position in the absence of the phantom. As discussed in Sec. 2.2.3, the backscatter factor B is given by the ratio

$$B = \frac{K_{\mathrm{a}}^{\mathrm{ph}}}{K_{\mathrm{a}}} \tag{3.5.1}$$

The equal result is obtained for the ratio of the corresponding air kerma rates, $\dot{K}_{\mathrm{a}}^{\mathrm{ph}}$ and $\dot{K}_{\mathrm{a}}$ if the irradiation conditions remain the same when determining each air kerma rate separately. A simplifying and approximative assumption is that the calibration coefficient N_{SFD} could be applied for the determination of the air kerma rate on-phantom analogous to Equ. 3.4.3 by

$$\dot{K}_{\mathrm{a}}^{\mathrm{ph}} \approx N_{\mathrm{SFD}} \cdot I_{\mathrm{SFD}}^{\mathrm{ph}} \tag{3.5.2}$$

When using a monitor, the ionization current I_{SFD} free-in-air or $I_{\mathrm{SFD}}^{\mathrm{ph}}$ on-phantom produced in the SFD is normalized to the monitor current I_{M} or $I_{\mathrm{M}}^{\mathrm{ph}}$ as discussed in Sec. 3.2.1. Since the air kerma rate is proportional to the ionization current produced in the monitor or in the SFD to a good approximation, the backscatter factor was calculated by

$$B = \frac{I_{\mathrm{SFD}}^{\mathrm{ph}}/I_{\mathrm{M}}^{\mathrm{ph}}}{I_{\mathrm{SFD}}/I_{\mathrm{M}}} \tag{3.5.3}$$

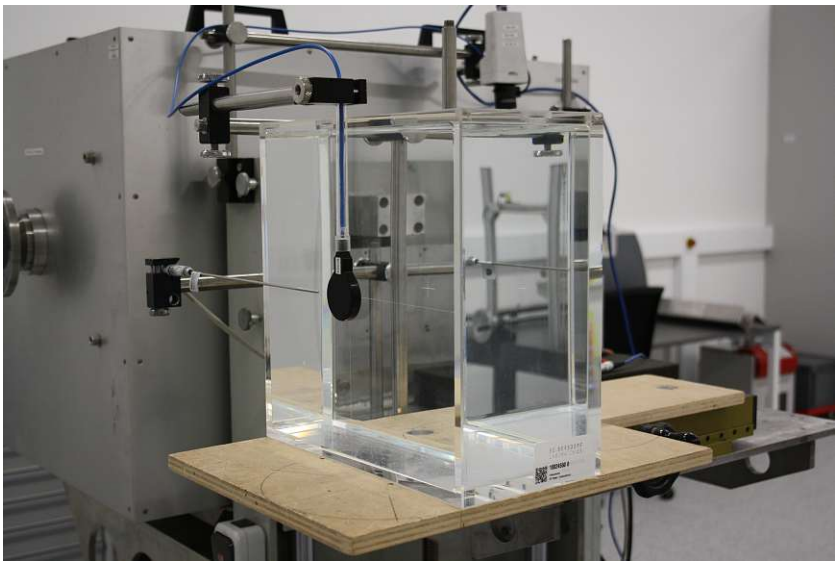

Figure 3.4: Experimental setup for measurements on the ISO slab using the SFD. Temperature in the closer environment of the chamber was measured using a temperature sensor (horizontally orientated sensor on the left).

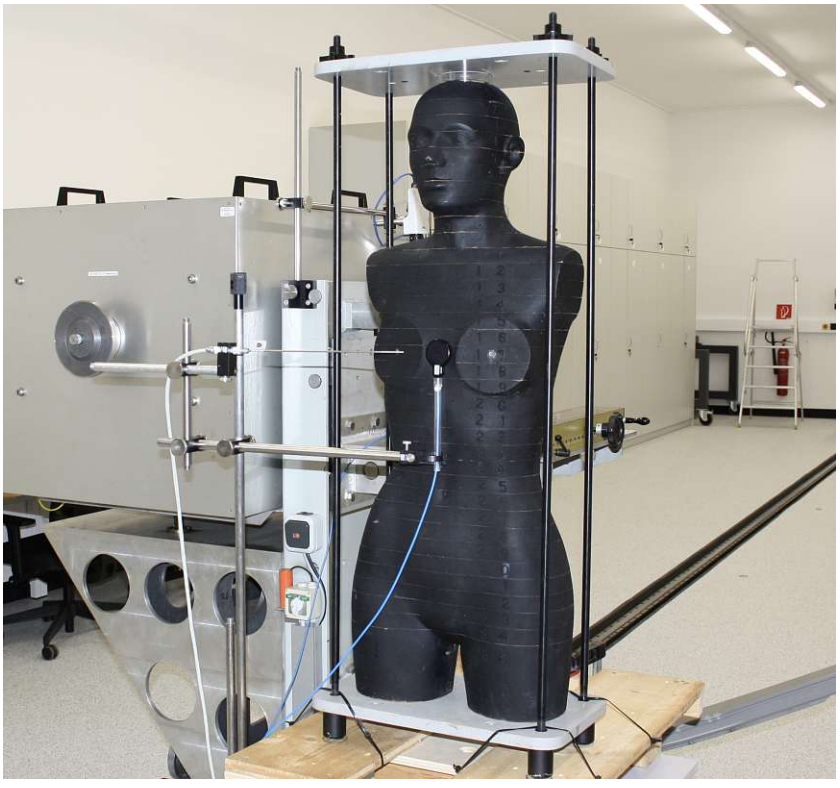

Figure 3.5: Experimental setup for measurements on the Alderson phantom using the SFD. Temperature in the closer environment of the chamber was measured using a temperature sensor (horizontally orientated sensor on the left).

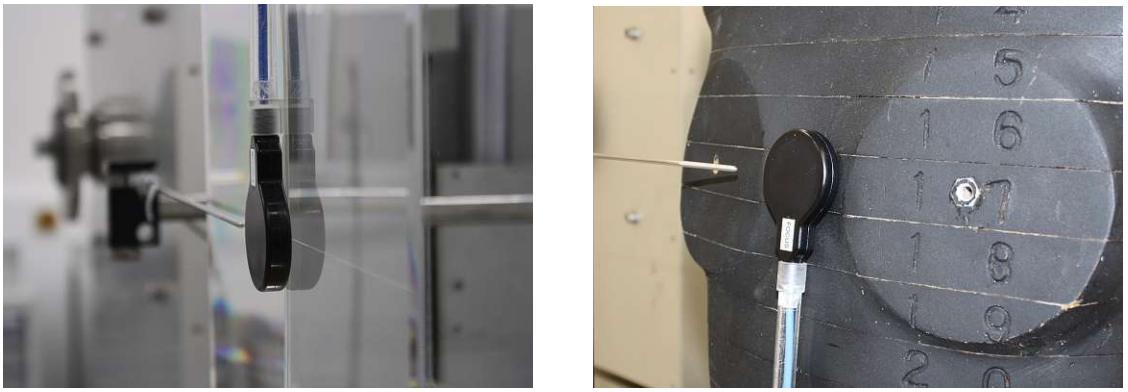

Figure 3.6: Close view of the SFD attached on the ISO slab (left) or on the Alderson phantom (right).

For each series of backscatter measurements on one of these two phantoms, the first run was carried out in presence of the phantom with the SFD placed directly at the reference point. Thus the measured ionization current $I_{\mathrm{SFD}}^{\mathrm{ph}}$ was the total of the incoming free-in-air fraction and the backscatter fraction resulting from the presence of the phantom.

Next, the phantom was removed with the SFD remaining on the exact same position and the measurement was repeated under the same irradiation conditions. The backscatter radiation contribution of the now measured current I_{SFD} omitted in these runs and the backscatter factor could therefore be calculated by simply applying Equ. 3.5.3.

3.5.1 Relative Backscatter Factors

The reference position on the Alderson phantom ('Pos0') for the detectors was chosen on the one hand because it represented an easy reproducible centered point at which the weak curvature of the surface allowed positioning of detectors almost side by side. On the other hand, it represented a realistic carrying position of dosemeters in the daily work routine. Since the exact carrying position is not mandatory, one has to consider the impact of position variations on the measurement results of the backscatter factor regarding our experimental setup. Three alternative carrying positions were selected (Fig. 3.7). 'Pos1' is in the same height as 'Pos0', but shifted to the left over the center of the right chest screw thread (slice 17). 'Pos2' is centered but shifted down by approximately 12 cm (slice 20). 'Pos3' is also centered but shifted up by approximately 12 cm (slice 14).

Measurements of the relative backscatter factor at the surface at 'Pos$X$' with $X = \{1, 2, 3\}$ with regard to the reference position 'Pos0' using the SFD were carried out. The relative backscatter factor is given by the ratio of the backscatter factors B^{PosX} at 'Pos$X$' and B^{Pos0} at 'Pos0':

$$\frac{B^{\mathrm{PosX}}}{B^{\mathrm{Pos0}}} = \frac{K_{\mathrm{a,ph}}^{\mathrm{PosX}} / K_{\mathrm{a}}^{\mathrm{PosX}}}{K_{\mathrm{a,ph}}^{\mathrm{Pos0}} / K_{\mathrm{a}}^{\mathrm{Pos0}}} \tag{3.5.4}$$

Air kerma at 'Pos0' and at 'Pos$X$' free-in-air was assumed to be approximately the same in that large distance from the focus, thus follows

$$K_{\mathrm{a}}^{\mathrm{PosX}} \approx K_{\mathrm{a}}^{\mathrm{Pos0}} \tag{3.5.5}$$

Equ. 3.5.4 could therefore be simplified to

$$\frac{B^{\mathrm{PosX}}}{B^{\mathrm{Pos0}}} \approx \frac{K_{\mathrm{a,ph}}^{\mathrm{PosX}}}{K_{\mathrm{a,ph}}^{\mathrm{Pos0}}} \tag{3.5.6}$$

The small error resulting from this approximation was within in the measurement uncertainty. Assuming a linear dependence of the ionization current of the SFD on the air kerma rate just like in the previous section and normalization of the currents $I_{\mathrm{SFD}}^{\mathrm{PosX}}$ to the monitor currents $I_{\mathrm{M}}^{\mathrm{PosX}}$, the relative backscatter factors were determined by

$$\frac{B^{\mathrm{PosX}}}{B^{\mathrm{Pos0}}} \approx \frac{I_{\mathrm{SFD}}^{\mathrm{PosX}} / I_{\mathrm{M}}^{\mathrm{PosX}}}{I_{\mathrm{SFD}}^{\mathrm{Pos0}} / I_{\mathrm{M}}^{\mathrm{Pos0}}} \tag{3.5.7}$$

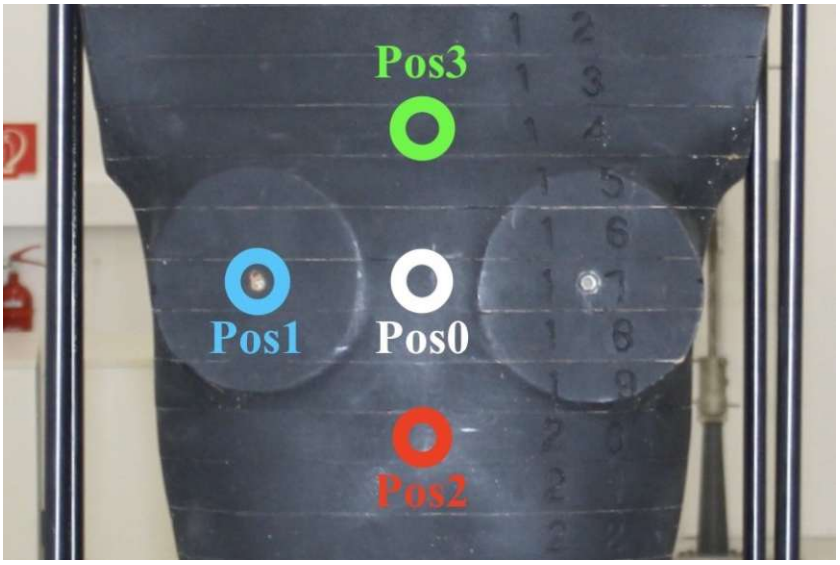

Figure 3.7: Selected positions for relative measurements on the Alderson phantom.

3.6 Measurement of the Response of EPD and TLD

For the EPD and the TLD the response regarding $H_p(10)$ was determined rather than backscatter factors. Deviations in the response depending on the choice of the phantom deliver information about the sensitivity of commonly used $H_p(10)$ dosemeters regarding backscatter radiation and thus the goodness of the representation of the real human body through the ISO water slab in practical personal dosimetry.

The calibrated monitor chamber was used to determine the rate $\dot{H}_p(10)$ in a distance of five meters from the focus and thus to calculate the irradiation time for a desired value of $H_p(10)$ on the surface of the ISO water slab. From the displayed dose of the EPD or the later evaluated result in case of the TLD, $[H_p(10)]_{\text{measured}}$, and the actually deposited dose, $[H_p(10)]_{\text{irradiated}}$, the response R is given by

$$R = \frac{[H_p(10)]_{\text{measured}}}{[H_p(10)]_{\text{irradiated}}} \tag{3.6.1}$$

The value for the response of the EPD was taken from a single irradiation, in case of the TLD a mean value of 2-10 TLD was evaluated.

Figure 3.8: EPD attached on the ISO slab reference position (left) or on the Alderson phantom reference position (right).

Figure 3.9: Four TLD attached on the ISO slab (left). TLD attached on the Alderson phantom (right). The result for the switched TLD served as additional information for the impact of carrying a TLD improperly and was not included into the calculations presented in this section.

Chapter 4

Computational Methods

For the backscatter simulations, the Monte Carlo Code MCNP6.2-EXE was used.

4.1 Kerma Approximation

In all simulations, the kerma approximation was assumed. Hereby, considering a photon interaction during which an electron is released, the energy is considered to be deposited locally at that point not including secondary electron transport, which saves a tremendous amount of time for Monte Carlo simulations. Especially in the range of radiology energies, emitted electrons generated in photon interactions have low energy and thus short ranges, this approximation gives good results. For photon energies above a few MeV where the assumption of the existence of charged-particle equilibrium is accurate the kerma approximation overestimates dose. Applying a thick-target bremsstrahlung model, the generation of bremsstrahlung is not automatically excluded when using the kerma approximation. Electrons are generated but slow to rest immediately at the point of generation under production of bremsstrahlung photons [22].

4.2 Development of the MCNP Model

All MCNP simulations were under usage of the kerma approximation, thus no electron transport was included in the calculations. The theoretical background of this approximation was pointed out in Sec. 4.1. Although electron transport was disabled, the simulations included bremsstrahlung generation using a thick-target bremsstrahlung model. Electrons are generated but locally slow to rest under production of photons.

The physics treatment also included Thomson scattering (coherent scattering), Compton scattering (incoherent scattering) and photoelectric absorption along with fluorescent photons and Auger effect. Again, produced electrons were treated with the thick target bremsstrahlung model and were assumed to deposit energy locally [18].

For the material compositions and densities, the NIST (National Institute of Standards and Technology) database was used. A summary of all used materials with their densities and elemental compositions is given in Table 4.1. In the special case of the calculations of the air kerma in cells with density near to zero (for example the 'vacuum' environment), the material 'Air*' was used. Cells in MCNP represent defined geometric entities with defined elemental composition and density. A negligible number of events (scattering, photoelectrical effect etc.) took place in these cells filled with Air*, which therefore shows equivalence to vacuum. The reason for this approach lay in the method of calculating air kerma, as explained in the next section, which is not applicable for void cells.

Material	Density ($g\ cm^{-3}$)	Element mass ratios					
		H	C	N	O	Al	Ar
Air	0,00120479	-	0,000124	0,755267	0,231781	-	0,012827
Air*	10^{-10}	-	0,000124	0,755267	0,231781	-	0,012827
Water	1,0	0,111894	-	-	0,888106	-	-
PMMA	1,19	0,080538	0,599848	-	0,319614	-	-
Graphite	0,32	-	1,0	-	-	-	-
Aluminium	2,69890	-	-	-	-	1,0	-
ICRU 4-element tissue	1,0	0,101172	0,111000	0,02600	0,761828	-	-

Table 4.1: Densities and elemental compositions of the materials used in backscatter simulations.

4.2.1 Calculation of Air Kerma and Absorbed Dose

Data for the mass energy-absorption coefficient $\left(\frac{\mu_{en}}{\rho}\right)$ for air and for ICRU 4-element tissue were obtained from [10], data for the bremsstrahlung radiation yield g_a in air were obtained directly from the ICRU upon request. Since a cubic Lagrange interpolation formula for the mass energy-absorption coefficient in air was once developed by members of the dosimetry laboratory and commonly used since then, we took over this data set. For the mass energy-absorption coefficient in ICRU 4-element tissue, we applied a cubic spine interpolation.

Among other methods, dose (air kerma or absorbed dose in tissue) can be calculated using the MCNP *f4-tally with appropriate 'dose functions'. The MCNP *f4 tally applied in air corresponds to the air kerma K_a, which approximately corresponds to the value of absorbed dose in case of electron equilibrium, at this certain point or volume considered. The 'dose functions' mentioned before correspond to the mass energy-transfer coefficients $\left(\frac{\mu_{tr}}{\rho}\right)$ in case of the calculation of air kerma or to the mass energy-absorption coefficients $\left(\frac{\mu_{en}}{\rho}\right)$ in case of the calculation of absorbed dose as a function of the photon energy E. This is also valid for any other material, for which this tally with appropriate dose functions was applied. For example, *f4 is used as an estimate for absorbed dose in case of the calculations of $H_p(10)$ in the following section.

Commonly used symbols in the following like K_a for air kerma and $H_p(10)$ for personal dose equivalent in context with MCNP simulations represent dose calculated using the *f4 tally.

4.2.2 Simulation of Conversion Coefficients from Air Kerma to Personal Dose Equivalent

The ratio of $H_p(10, \alpha)$ in 10 mm depth of the ICRU 4-element tissue phantom to the air kerma K_a at this point in absence of the phantom gives the conversion coefficient $h_{pK}(10, \alpha)$ for an angle of radiation incidence α:

$$h_{pK}(10, \alpha) = \frac{H_p(10, \alpha)}{K_a} \tag{4.2.1}$$

Data for the conversion coefficients from air kerma or fluence to any operational dose quantity for monoenergetic radiation are provided by the ISO (International Organisation for Standardization) for monoenergetic radiation and certain standardized spectra [21].

For the re-calculation of the conversion coefficients we selected a sensitive cuboid volume inside the ICRU tissue phantom in 10 mm depth in case of the calculation of $H_p(10)$. The dimensions of 2 mm × 0,4 mm × 2 mm (0,4 mm is the thickness of the detector in the direction of radiation incidence) were large enough to obtain a sufficiently small statistical uncertainty and small enough to actually calculate dose in 10 mm depth and not an average over a large volume, which would not have given necessarily the same value. The value for the air kerma at that point in absence of the phantom was calculated for the same detector geometry. The radiation beam was broad and parallel as required according to the ICRP.

4.2.3 Calculation of Backscatter Factors

MCNP provides an useful tool, the 'cell flagging', with whose help the air kerma generated in a certain volume solely produced by photons scattered in 'flagged' objects in the environment and subsequently entering the detector volume could be calculated separately. On the one hand, we obtain the total air kerma K_a^{tot} produced by all photons and on the other hand the air kerma K_a^{back} produced by the scattered photons from flagged objects, for example the phantom, into the detector volume considered.

We considered a cuboid 'ideal detector' in the center of the ISO water slab surface facing the radiation source with dimensions 6 mm × 2 mm × 6 mm with the flat side parallel to the phantom surface. The backscatter factor could be calculated by

$$B = \frac{K_a^{tot}}{K_a^{tot} - K_a^{back}} \tag{4.2.2}$$

The ratio of air kerma produced by backscattered photons from the phantom could therefore be excluded by subtraction of $K_a^{tot} - K_a^{flag}$, which corresponds to the air kerma free-in-air, if we consider no other objects than the phantom representing scattering objects.

4.2.3.1 Dependence on Radiation Beam Geometry

The Monte Carlo method is perfectly suited for the fast determination of the effect of certain influences such as geometric variations of the radiation source like distance from the detector, solid angle of the beam, degree of illumination of the phantom etc.

Since the backscatter factor B is slightly dependent on the radiation beam geometry, we again considered the cuboid 'ideal detector' in the center of the ISO water slab surface facing the radiation source (monoenergetic 60 keV or for the N-80 X-ray spectrum, which serves as a reference spectrum for many calculations in the following). Calculations of backscatter factors $B_{parallel}$ in case of a broadened parallel radiation beam incident on the phantom or B_{point} in case of a point source which is positioned five meters from the phantom's surface, which corresponds to the measurement conditions in the experiments, were performed. In both situations, the ISO slab was completely illuminated (Fig. 4.1).

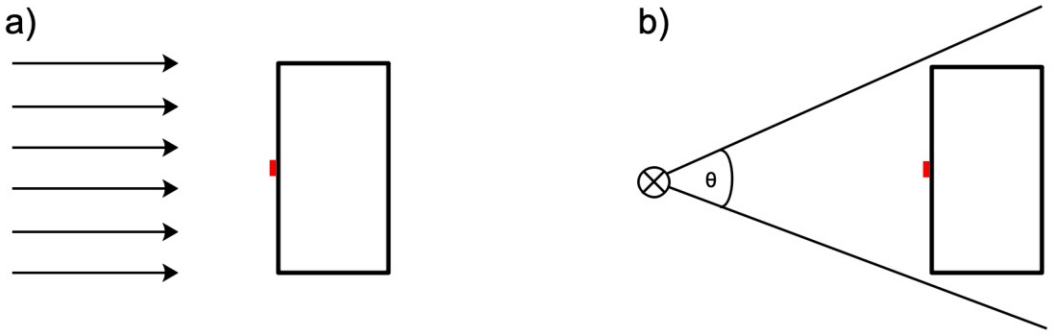

Figure 4.1: Schematic of the geometrical conditions in the backscatter simulations on the ISO water slab using the ideal detector (red) for **a)** broadened parallel radiation beam **b)** cone-shaped radiation beam with solid angle θ starting from a point source in five meters distance from the slab's surface.

4.2.4 Modeling the SFD

The MCNP model of the SFD ionization chamber represented a simplified version of the real SFD since it was built cylindrical (Fig. 4.2) under neglect of the PMMA extension at the lower part, where the cables enter the chamber (Fig. B.1). Furthermore, the narrow gap between the SFD and the phantom surface was neglected.

The interior of the SFD was simulated in detail according to the construction plan. Starting from the outside, the outer chamber walls are built of PMMA. A graphite coating is applied on the inner walls of the cavities, which are filled with air. The partition in the middle is the electrode, which consists of a PMMA layer coated with graphite with an aluminium foil on both sides.

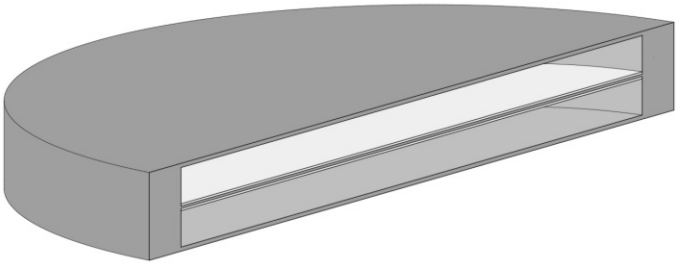

Figure 4.2: Illustration of the geometry of the cylindrical SFD ionization chamber model used in the simulations. In this picture, the material PMMA is shown in grey and aluminium in white.

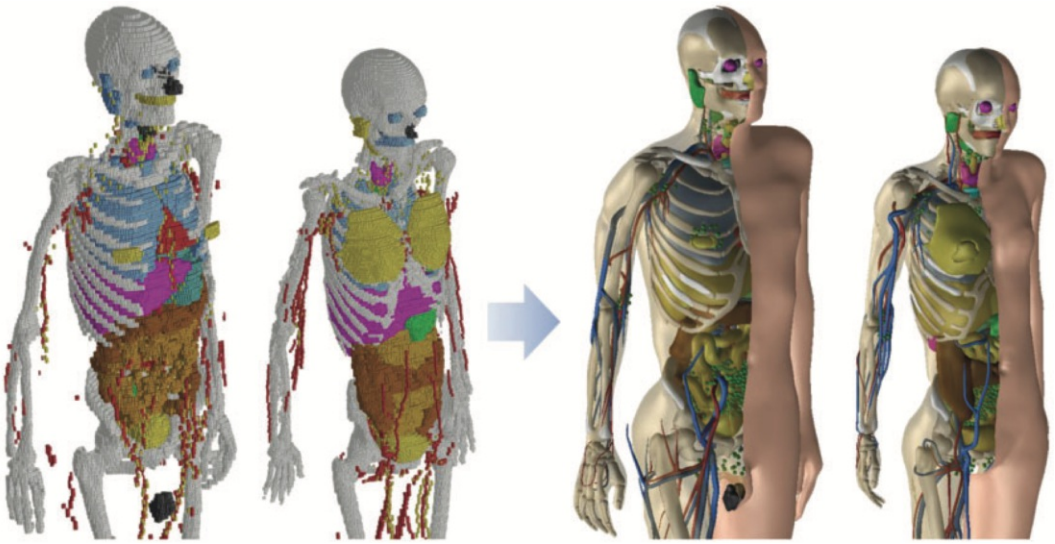

Figure 4.3: Voxel-type ICRP reference phantoms (left) and the new mesh-type reference phantoms (MRCPs) (right) [24].

4.3 Adult Mesh-Type Reference Computational Phantoms (MRCPs)

The phantoms presented in the ICRP *Publication 110* [15] are currently the official computational phantoms following the recommendations for the Reference Female and Reference Male introduced in ICRP *Publication 103* [12] and are consistent with ICRP *Publication 89* [16], which gives reference organ and tissue masses and dimensions. Based on computed tomographic data of real people, the models were implemented through segmentation to a three-dimensional voxel phantom as the most detailed representation of the human body at the present time. However, small structures like thin layers could not be resolved adequately, which is why the adult mesh-type reference computational phantoms (MRCPs) were developed by the ICRP by conversion of the voxel-phantoms to a high resolution mesh format and completion of tissue and tissue layers associated with radiogenic cancer risk which could not be resolved in the voxel phantoms [23, 24]. These MRCPs include structures in the µm range, so effective dose can be estimated in a more accurate and more precise manner.

Under consideration of these advantages, a study of backscattering on the human body should also be done under usage of the more realistic MRCPs. These were kindly provided by the Hanyang University Radiation Engineering Laboratory (HUREL) at Hanyang University in Seoul, Korea.

4.3.1 Simulation of Backscatter Factors on the Male MRCP

Since the male MRCP does not represent the exact computational implementation which corresponds to the Alderson phantom used in the measurements, the simulation of backscatter factors can not be seen as a one-to-one simulation of the measurements. Thus, the SFD chamber was not used here and an ideal cuboid detector with the dimensions 1 cm × 0,5 cm × 1 cm served as detector volume. This is similar to the detector used for the calculations of ideal backscatter factors on the ISO water slab.

The flat side was as parallel and as close as possible to the region of the MRCP surface which corresponds approximately to the position of the sternum, facing the radiation point source in five meters distance which was in the same height as the detector.

Due to the concave and irregular surface curvature, the detector could not be placed exactly side by side with the phantom without overlapping. To evaluate the closest approach of the detector to the phantom surface in direction of radiation incidence, the coordinates of the most external organ, the 'insensitive skin of the trunk', were considered, limited to the range of height (z-range) in which the detector should be placed (z =[39 cm, 41 cm]). In other words, a 'slice' of the body that only contains the insensitive skin of the trunk was taken, whereby every single coordinate of the tetrahedral geometry is given. Therewith, the coordinates of closest approach to the three dimensional topography could be determined (Fig. 4.4).

The backscatter factor B was then calculated analogous to Equ. 4.2.2 using the MCNP cell flagging tool.

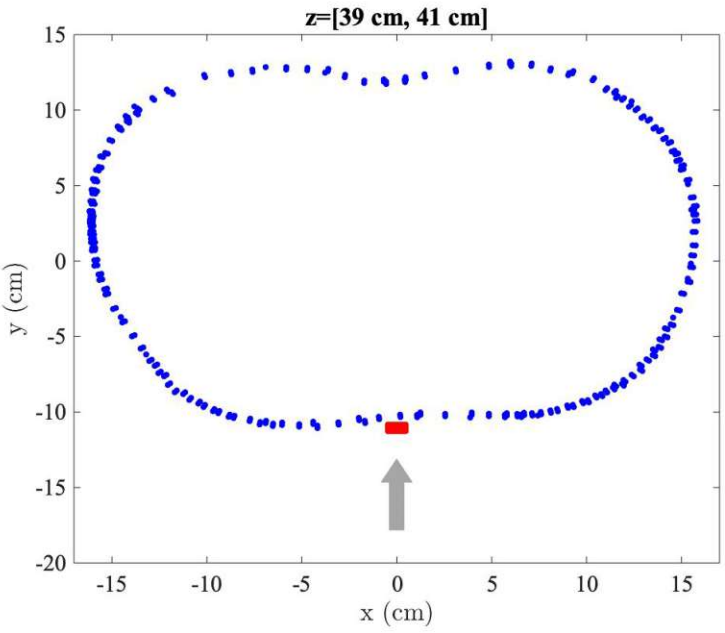

Figure 4.4: x and y coordinates of the MRCP 'insensitive skin of the trunk' (blue dots) and of the cuboid detector (red) positioned at the sternum. The grey arrow indicates the direction of radiation incidence from a point source in five meters distance from the surface in which the MRCP was oriented.

Chapter 5

Results and Discussion

The expanded uncertainty $U = U(k = 2)$ with coverage factor k given in the following defines an interval estimated to have a level of confidence of 95 %.
Data points in graphics were interpolated using a cubic spline interpolation formula.

5.1 Simulated Conversion Coefficients from Air Kerma to Personal Dose Equivalent

Results of MCNP simulations for the conversion coefficient $h_{\mathrm{pK}}(10, \alpha)$ from air kerma K_{a} to personal dose equivalent $H_{\mathrm{p}}(10, \alpha)$ are tabulated for various photon energies and angles of incidence in Tab. 5.1 and Tab. 5.2, together with the values published by the ICRP [25]. The re-calculation of these coefficients served as validation of the methods applied in our backscatter simulations.

E (keV)	$h_{\mathrm{pK}}(10, 0°)$ (simulated)	U	$h_{\mathrm{pK}}(10, 0°)$ (ICRP74)	deviation
40	1,516	1,1 %	1,490	1,8 %
60	1,898	1,0 %	1,892	0,3 %
80	1,911	1,0 %	1,903	0,4 %
100	1,815	0,9 %	1,811	0,2 %

Table 5.1: Simulated conversion coefficients $h_{\mathrm{pK}}(10, 0°)$ from air kerma K_{a} to personal dose equivalent $H_{\mathrm{p}}(10, 0°)$ with expanded uncertainty $U(k = 2)$ for photon energy E and their deviation relative to the ICRP values.

All deviations were in an acceptable extent and thus the MCNP model could be assessed to be accurate, and along with this the usage of approximations could be justified. It should be noted that for the calculations performed by the ICRP

E=60 keV	$h_{pK}(10,\alpha)$ (simulated)	U	$h_{pK}(10,\alpha)$ (ICRP74)	deviation
0°	1,898	1,0 %	1,892	0,3 %
15°	1,893	1,2 %	1,869	1,3 %
30°	1,843	1,3 %	1,833	0,5 %
45°	1,715	1,2 %	1,724	-0,5 %

Table 5.2: Simulated conversion coefficients $h_{pK}(10,\alpha)$ from air kerma K_a to personal dose equivalent $H_p(10,\alpha)$ with expanded uncertainty $U(k=2)$ for angle of incidence α and photon energy $E = 60$ keV and their deviation relative to the ICRP values.

probably different detector geometries were used. This can lead to intrinsic deviations solely caused by differently chosen geometry and not by fundamentally wrong approaches in our MCNP model.

5.2 Impact of the Radiation Beam Geometry on Backscatter Factors

Tab. 5.3 shows differences in backscatter factors for a broad parallel beam and for a realistic broad beam starting from a point source in five meters distance (Fig. 4.1 a) and b), respectively). A clear difference in the backscatter factor in case of the parallel beam irradiation relative to the diverging beam of approximately -2 % could be attributed solely to the different geometry of the incident radiation beam.

One has to consider this essential difference with regard to the definition of the personal dose H_p, where the conversion coefficient is calculated for broad parallel beams which was obviously not the case in our experimental setup. These exemplary simulations therefore indicate a degree of violation of this requirement when consulting measured dose or backscatter factors when using tabulated H_p conversion coefficients.

E (keV) or quality	$B_{parallel}$	$B_{diverging}$	$\frac{B_{parallel}}{B_{diverging}}$	U
60	1,688	1,719	0,982	0,5 %
N-80	1,668	1,699	0,982	0,5 %

Table 5.3: Comparison of the backscatter factor in case of a broad parallel beam, $B_{parallel}$, and in case of a diverging beam starting from a point source in five meters distance, B_{point}, with expanded uncertainty $U(k=2)$.

The calculated backscatter factor for 60 keV could be compared to the result in [26] for a 35 cm × 35 cm square field originating from a point source in one meter distance, where a value of 1,692 with an estimated combined standard uncertainty of 1 % is indicated. Our result for the parallel beam deviated by -0,2 % and lied within the limits of uncertainty, the calculated backscatter factor for the point source in five meters distance by 1,6 %. In [27], a backscatter factor of 1,70 for a 25 cm × 25 cm square field originating from a point source in 1,5 meters distance was calculated with an uncertainty of less than 1 %. Deviations to this value were -0,6 % in case of the parallel beam and 1,2 % in case of the diverging beam.

For the backscatter factor of 1,686 calculated in [28] for a point source in slightly above one meter distance from the ISO slab surface, the deviations were 0,1 % and 2 %. However, there was no specification of uncertainty given.

5.3 Backscatter Profile and Backscatter Spectra on the ISO Water Slab

5.3.1 Backscatter Profile

Calculations of the spacial distribution of the air kerma and the backscatter factor on the phantom surface and in the area in front of it using a MCNP mesh tally were performed for the ISO water slab. For this a lattice of cuboid vacuum cells with the dimensions of $x \times y \times z = 0{,}4$ cm × 0,4 cm × 0,2 cm with cell numbers $N_x = 75$, $N_z = 75$ in x- or z-direction was applied on the surface facing the N-80 point source in five meters distance, so the area was congruent to the phantom surface being 30 cm × 30 cm.

One can recognize decisive differences in the surface distribution of air kerma in Fig. 5.1 and Fig. 5.2 for the used N-80 X-ray spectrum. Applying the criterion of a maximum variation of ±5 % of the air kerma on the surface to limit an effective usable area for irradiating dosemeters on the ISO slab like recommended in [19], we can graphically display this area in the color mesh plots. Obviously, detectors for determining the air kerma on the surface of the ISO slab for calibrating purposes with angle of incidence of 0° should only be applied right in the middle with a maximum displacement of approximately 10 cm to obtain comparable and meaningful results. In case of 60° angle of incidence, which is the required angular range for personal dosimeter with the detector applied right in the center of the surface, this effective usable area is greatly reduced.

The same simulations were used for the calculation of the backscatter factor

distribution on the slab surface (Fig. 5.3 and Fig. 5.4). These plots point out the importance of the consistent positioning of the detector when measuring backscatter factors due to the strong decrease towards the edges. In case of an angle of incidence of 60°, the maximum backscatter factor at the surface is even shifted towards the edge next to the source.

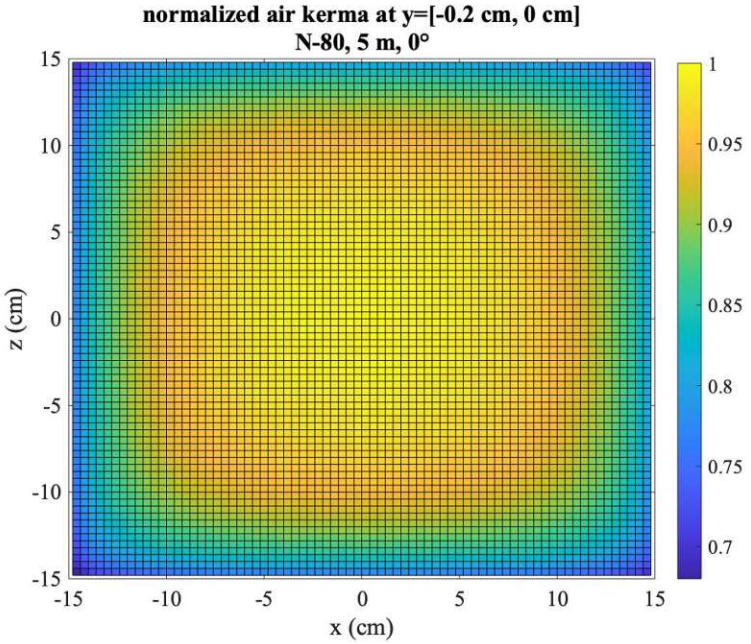

Figure 5.1: Color mesh plot of normalized air kerma on the surface of the ISO slab facing the N-80 point source with an angle of incidence of 0° to the y-axes in a distance of five meters from the focus.

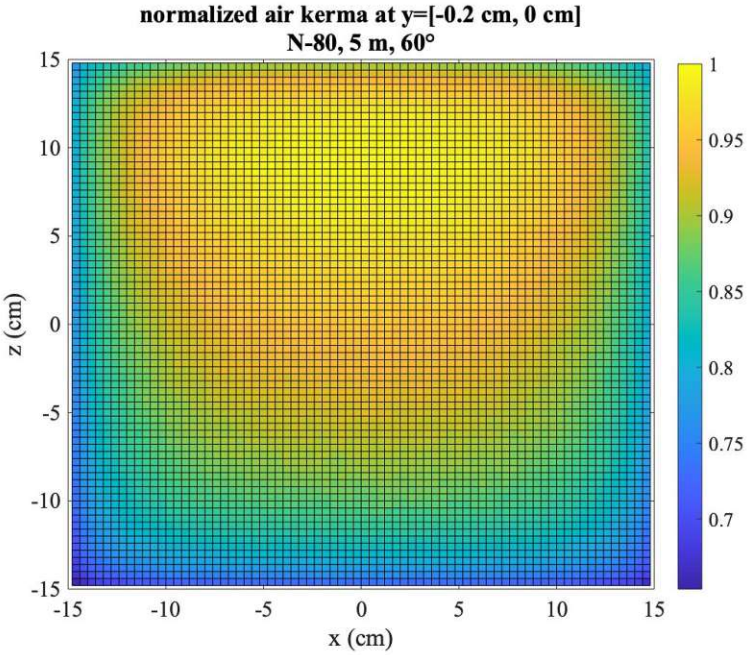

Figure 5.2: Color mesh plot of normalized air kerma on the surface of the ISO slab facing the N-80 point source with an angle of incidence of 60° to the y-axes in a distance of five meters from the surface center to the focus.

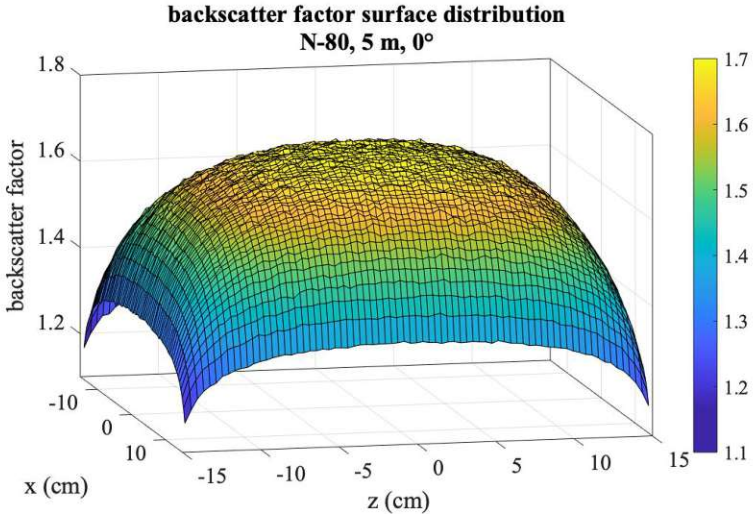

Figure 5.3: Color surface plot of the backscatter factor distribution on the surface of the ISO slab facing the N-80 point source with an angle of 0° to the y-axes in a distance of five meters from the focus.

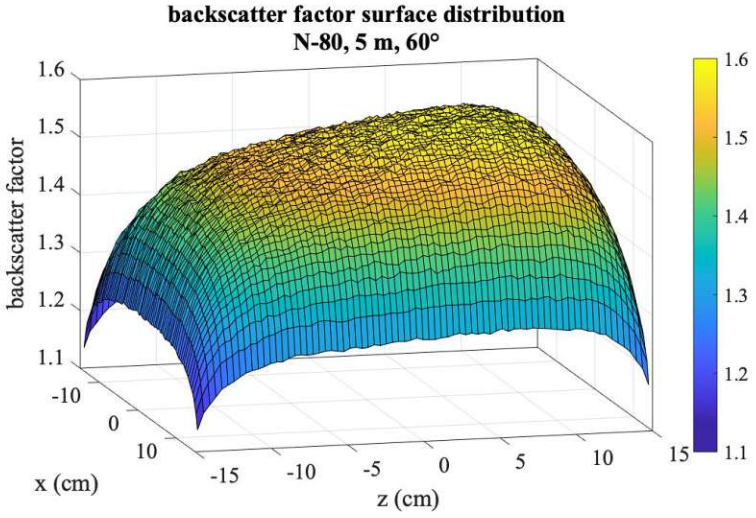

Figure 5.4: Color surface plot of the backscatter factor distribution on the surface of the ISO slab facing the N-80 point source with an angle of 60° to the y-axes in a distance of five meters from the focus.

5.3.2 Backscatter Spectrum

Air kerma spectra produced by incident and backscattered photons were calculated separately during all simulations of the backscatter factor. As representative incident spectra for the figures in the following, monoenergetic 60 keV radiation and the N-80 spectrum were chosen. The unattenuated total and backscattered spectrum was calculated for the cuboid vacuum 'point detector' as described in Sec. 4.2. In the same manner, the spectra inside the SFD ionization chamber could also be calculated whereby the chamber hull acts as a filter for the radiation. To justify the designation 'shadow free' of this chamber to be actually true, the attenuating and filtering effect should be sufficiently weak in the energy range specified by the manufacturer.

Fig. 5.5 to Fig. 5.7 each show the incident, backscattered and total air kerma spectrum for the ideal point detector and the SFD. In case of the SFD, the presence of the chamber wall showed its weak influence. In the range 50 keV to 70 keV, the total spectrum was reduced by a maximum of approximately 5 % compared to the point detector, whereby it is to mention here that the detector geometry was significantly different which could also account for a certain proportion. Overall, however, it could be argued that the SFD reproduced a value close to that of an ideal point detector.

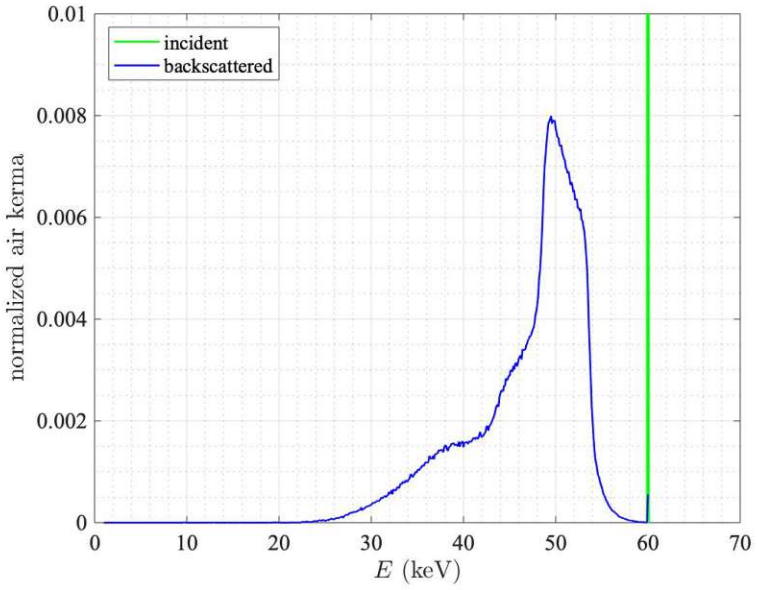

Figure 5.5: Air kerma spectrum produced by incident and backscattered photons with energy E in the point detector on the ISO water slab for a 60 keV monochromatic source.

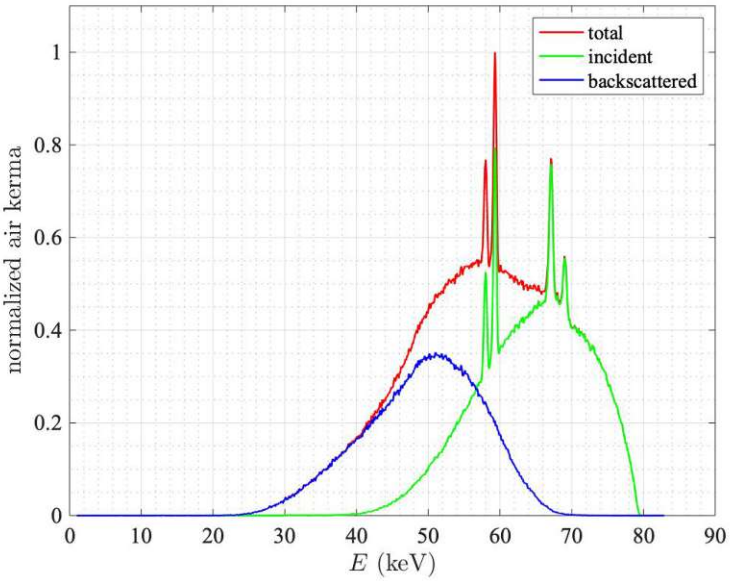

Figure 5.6: Air kerma spectrum produced by incident and backscattered photons with photon energy E and total air kerma spectrum in the point detector on the ISO water slab for radiation quality N-80.

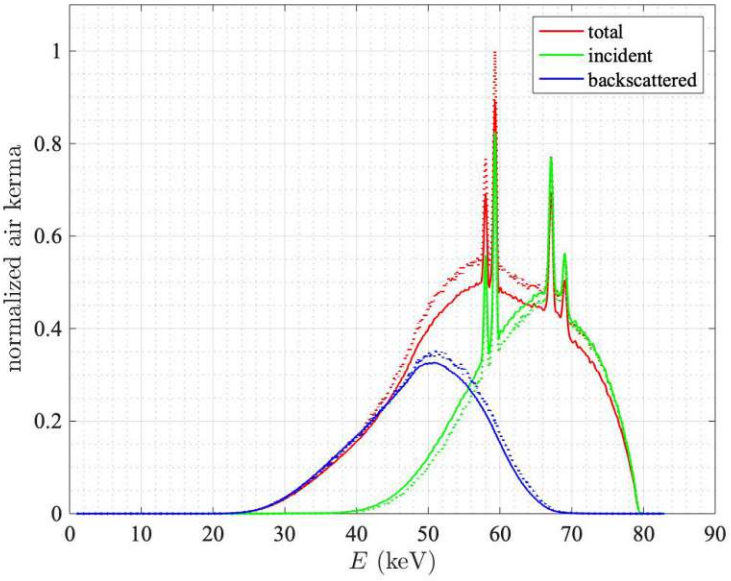

Figure 5.7: Air kerma spectrum produced by incident and backscattered photons with photon energy E and total air kerma spectrum inside the SFD on the ISO water slab for radiation quality N-80. The dotted lines represent the unattenuated spectra calculated for the point detector.

5.4 Backscatter Factors on the ISO Water Slab

5.4.1 Simulations Using the Point Detector and the SFD

Simulations using the point detector were performed to obtain ideal backscatter results with no influences like filtration and scattering on a detector wall and the averaging over a larger volume associated with the detector geometry (Tab. 5.4). A significant decrease of the backscatter factor could be seen in the results when using the SFD detector geometry (Tab. 5.5), which was simulated to allow a direct comparison with the folllwing measurement results. In both cases, the radiation beam startet from a point source in five meters distance from the phantom's surface similar to the measurement setup.

The deviations in backscatter factors of the SFD to the ideal detector show the influence of the chamber geometry and its walls and can be used to determine a correction factor for that chamber.

radiation quality	$\overline{E}_{K_a}$ (keV)	$B_{\text{point}}(0°)$	U	$B_{\text{point}}(30°)$	U	$B_{\text{point}}(60°)$	U
N-30	23,7	1,202	0,3 %	1,197	0,3 %	1,172	0,3 %
N-40	32,3	1,369	0,4 %	1,357	0,4 %	1,302	0,4 %
N-60	46,5	1,607	0,5 %	1,587	0,5 %	1,485	0,5 %
N-80	64,4	1,699	0,5 %	1,676	0,5 %	1,564	0,5 %
N-100	83,1	1,641	0,5 %	1,623	0,5 %	1,528	0,4 %
N-120	100,8	1,561	0,2 %	1,550	0,4 %	1,474	0,4 %
N-150	120,6	1,483	0,4 %	1,476	0,4 %	1,425	0,4 %

Table 5.4: Simulated backscatter factors $B_{\text{point}}(\alpha)$ on the ISO water slab with expanded uncertainty $U(k = 2)$ for an angle of incidence of α for the point detector.

radiation quality	$\overline{E}_{K_a}$ (keV)	$B_{\text{SFD}}(0°)$	U	$B_{\text{SFD}}(30°)$	U	$B_{\text{SFD}}(60°)$	U
N-30	23,7	1,163	0,2 %	1,160	0,3 %	1,141	0,2 %
N-40	32,3	1,317	0,3 %	1,309	0,2 %	1,261	0,3 %
N-60	46,5	1,538	0,4 %	1,519	0,3 %	1,432	0,3 %
N-80	64,4	1,626	0,4 %	1,603	0,3 %	1,508	0,3 %
N-100	83,1	1,578	0,3 %	1,560	0,3 %	1,480	0,3 %
N-120	100,8	1,503	0,2 %	1,492	0,2 %	1,433	0,3 %
N-150	120,6	1,436	0,3 %	1,429	0,2 %	1,385	0,3 %

Table 5.5: Simulated backscatter factors $B_{\text{SFD}}(\alpha)$ with expanded uncertainty $U(k = 2)$ for an angle of incidence of α using the SFD on the ISO water slab.

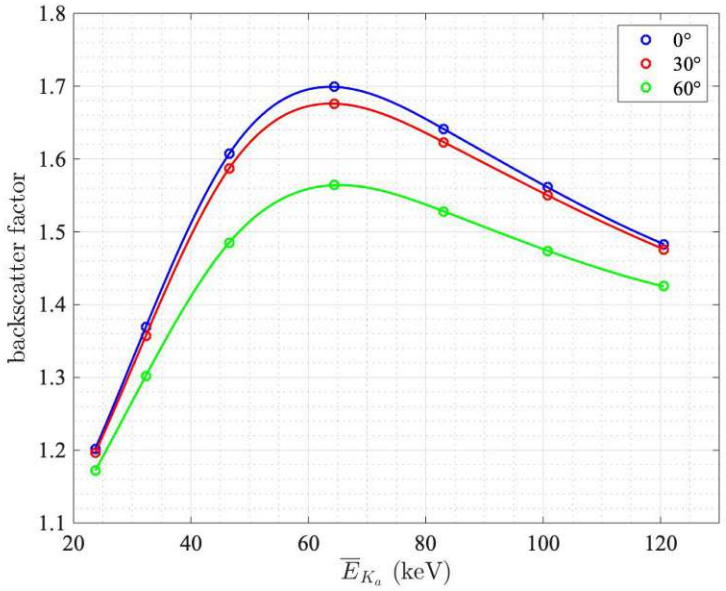

Figure 5.8: Simulated backscatter factors as a function of the spectrum's mean energy in keV on the ISO water slab for perpendicular incidence, 30° or 60° angle of incidence of in a distance of five meters from the focus for the point detector.

5.4.2 Measurements Using the SFD

The backscatter measurement results are shown in Tab. 5.6 and Fig. 5.9 to 5.11.

radiation quality	$\overline{E}_{K_a}$ (keV)	$B(0°)$	U	$B(30°)$	U	$B(60°)$	U
N-30	23,7	1,161	0,5 %	1,158	0,6 %	1,126	0,5 %
N-40	32,3	1,299	0,4 %	1,299	0,5 %	1,244	0,4 %
N-60	46,5	1,537	0,3 %	1,520	0,1 %	1,424	0,3 %
N-80	64,4	1,625	0,3 %	1,607	0,2 %	1,504	0,2 %
N-100	83,1	1,553	0,5 %	1,542	0,2 %	1,456	0,2 %
N-120	100,8	1,462	0,5 %	1,471	0,4 %	1,405	0,3 %
N-150	120,6	1,420	1,4 %	1,421	0,4 %	1,376	0,2 %

Table 5.6: Measured backscatter factors $B(\alpha)$ with expanded uncertainty $U(k = 2)$ for an angle of incidence of α using the SFD on the ISO water slab.

5.4.3 Comparison of Simulation and Measurement

Tab. 5.7 and Fig. 5.9 to Fig. 5.11 summarize the results from measurements and simulations of the backscatter factor using the SFD.

radiation quality	$\overline{E}_{K_a}$ (keV)	B_{SFD}/B $\alpha = 0°$	$\alpha = 30°$	$\alpha = 60°$
N-30	23,7	0,0 %	-0,1 %	1,3 %
N-40	32,3	1,4 %	0,7 %	1,4 %
N-60	46,5	0,0 %	-0,1 %	0,5 %
N-80	64,4	0,1 %	-0,2 %	0,3 %
N-100	83,1	1,6 %	1,1 %	1,6 %
N-120	100,8	2,8 %	1,5 %	2,0 %
N-150	120,6	1,1 %	0,6 %	0,6 %

Table 5.7: Deviation in per cent of simulated backscatter factors $B_{SFD}(\alpha)$ on the ISO water slab for the SFD compared to measured backscatter factors $B(\alpha)$, for an angle of incidence α of 0°, 30° and 60°.

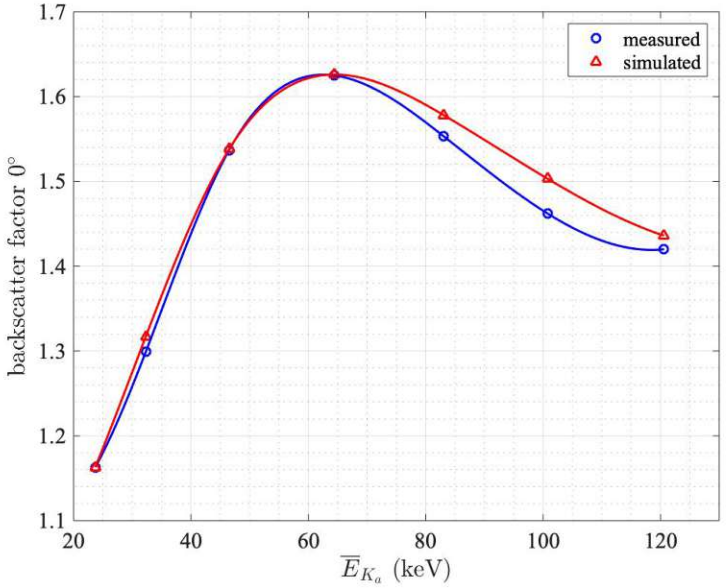

Figure 5.9: Comparison of simulated and measured backscatter factors using the SFD as a function of the spectrum's mean energy $\overline{E}_{K_a}$ in keV on the ISO water slab for perpendicular incidence in a distance of five meters from the focus.

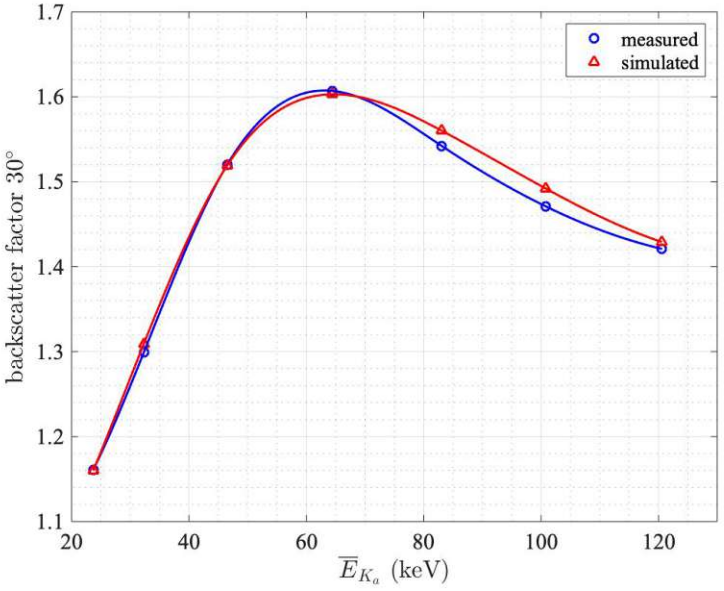

Figure 5.10: Comparison of simulated and measured backscatter factors using the SFD as a function of the spectrum mean energy $\overline{E}_{K_a}$ in keV on the ISO water slab for an angle of incidence of 30° in a distance of five meters from the focus.

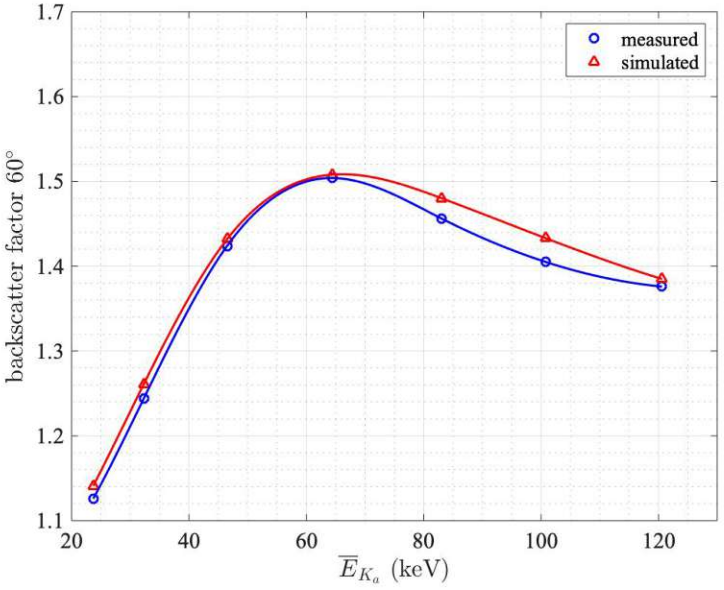

Figure 5.11: Comparison of simulated and measured backscatter factors using the SFD as a function of the air kerma spectrum mean energy $\overline{E}_{K_a}$ in keV on the ISO water slab for an angle of incidence of 60° in a distance of five meters from the focus.

For each angle the same characteristic could be seen. In the lower energy range up to including 83,1 keV the simulation results matched very well with a maximum deviation of the simulation to the measurement of $1,6$ %. For the next quality higher in its mean energy, 100,8 keV, we had the highest deviation, consistent for every single angle. Nevertheless, the deviations were acceptable in their extent themself and did not cause concerns since the curves converge again in the next higher step in energy. Thus, possible influences were not further investigated and the MCNP model could be considered to be sufficiently accurate.

Possible influences that could cause deviations were scattering effects on objects or in the air around the measurement setup, which were not taken into account in the simulations. Also, the generated radiation field of an X-ray tube is never completely homogeneous in reality, but very well in the MCNP model.

5.5 Simulated Backscatter Factors on the ICRU Tissue Slab Phantom

As before, the point source was located at a distance of five meters from the phantom's surface.

radiation quality	$\overline{E}_{K_a}$ (keV)	$B_{\text{point}}(0°)$	U	$B_{\text{point}}(60°)$	U
N-30	23,7	1,191	0,3 %	1,156	0,3 %
N-40	32,3	1,364	0,4 %	1,292	0,4 %
N-60	46,5	1,609	0,5 %	1,483	0,5 %
N-80	64,4	1,699	0,5 %	1,562	0,5 %
N-100	83,1	1,640	0,5 %	1,532	0,5 %
N-120	100,8	1,556	0,4 %	1,473	0,4 %
N-150	120,6	1,480	0,4 %	1,425	0,4 %

Table 5.8: Simulated backscatter factors $B_{\text{point}}(\alpha)$ on the ICRU 4-element tissue slab with expanded uncertainty $U(k = 2)$ dependent on angle of incidence of α for the point detector.

Comparing the simulated backscatter factors on the ISO water slab and the ICRU 4-element tissue slab for 0° and 60°, we can verify their equivalence of backscatter behavior (Tab. 5.8) and Fig. 5.12). Additionally, we can make an important predicition regarding to the measurements with the Alderson phantom. Assuming material composition of the Alderson similar to ICRU 4-element tissue, the differences be-

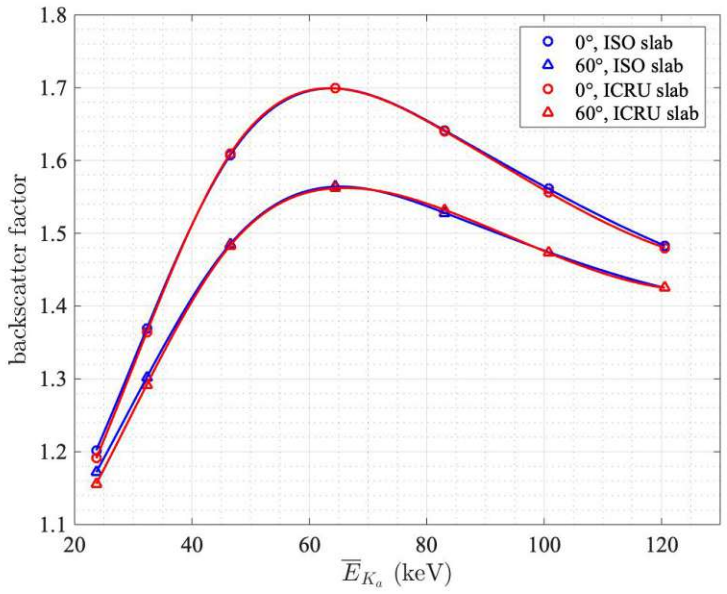

Figure 5.12: Comparison of simulated backscatter factors as a function of the spectrum's mean energy $\overline{E}_{K_a}$ in keV on the ICRU slab or the ISO water slab, for perpendicular incidence or 60° an angle of incidence in a distance of five meters from the focus for the point detector.

tween the backscatter factors of the ISO water slab calibration phantom and the Alderson phantom actually derive almost exclusively from their different geometry.

5.6 Backscattering on the Alderson Phantom

It should be noted that attachments provided for the Alderson phantom which represented differently shaped female breasts were not applied. This was done to ensure that the Alderson phantom represented a body that was as gender neutral as possible and thus included the most generally usable case.

5.6.1 Backscatter Factors for Reference Position

Tab. 5.9 shows measured backscatter factors using the SFD on the Alderson phantom at the personal detector position (reference position, 'Pos0').

radiation quality	$\overline{E}_{K_a}$ (keV)	$B(0°)$	U	$B(30°)$	U	$B(60°)$	U
N-30	23,7	1,160	0,4 %	1,163	0,4 %	1,135	0,2 %
N-40	32,3	1,359	0,7 %	1,345	0,3 %	1,283	0,7 %
N-60	46,5	1,552	0,1 %	1,534	0,4 %	1,453	0,3 %
N-80	64,4	1,593	0,1 %	1,577	0,4 %	1,489	0,4 %
N-100	83,1	1,497	0,3 %	1,487	0,5 %	1,419	0,7 %
N-120	100,8	1,413	0,2 %	1,414	0,5 %	1,365	1,0 %
N-150	120,6	1,364	0,4 %	1,354	0,3 %	1,338	0,5 %

Table 5.9: Measured backscatter factors $B(\alpha)$ on the Alderson phantom (reference position, 'Pos0') with expanded uncertainty $U(k = 2)$ dependent on the angle of incidence α using the SFD chamber.

5.6.2 Relative Backscatter Factors for Various Detector Positions

The superscripts 'Pos1' to 'Pos3' correspond to the designations for the selected alternative carrying positions for dosimeters as shown in Chap. 3, Fig. 3.7. 'Pos0' corresponds to the reference personal detector position at which the backscatter factors in the previous section were measured. Results are summarized in Tab. 5.10 and graphically displayed in Fig. 5.13.

radiation quality	$\overline{E}_{K_a}$ (keV)	$\frac{B^{\mathrm{Pos1}}}{B^{\mathrm{Pos0}}}$	U	$\frac{B^{\mathrm{Pos2}}}{B^{\mathrm{Pos0}}}$	U	$\frac{B^{\mathrm{Pos3}}}{B^{\mathrm{Pos0}}}$	U
N-40	32,3	0,990	0,4 %	1,040	0,5 %	0,984	0,5 %
N-60	46,5	0,969	0,3 %	1,046	0,2 %	0,995	0,2 %
N-80	64,4	0,957	0,1 %	1,044	0,2 %	0,998	0,2 %
N-100	83,1	0,959	0,3 %	1,040	0,4 %	1,004	0,6 %
N-120	100,8	0,967	0,2 %	1,034	0,3 %	1,005	0,4 %

Table 5.10: Measured relative backscatter factors on the Alderson phantom for various dosemeter carrying positions with regard to the reference position with expanded uncertainty $U(k = 2)$ for perpendicular incidence of radiation using the SFD chamber.

A longitudinal or medial position variation of the detector by approximately 12 cm can make a difference of up to $\approx$ 5 % in measured air kerma using the SFD ionization chamber. The radiation field was considered to be homogeneous at

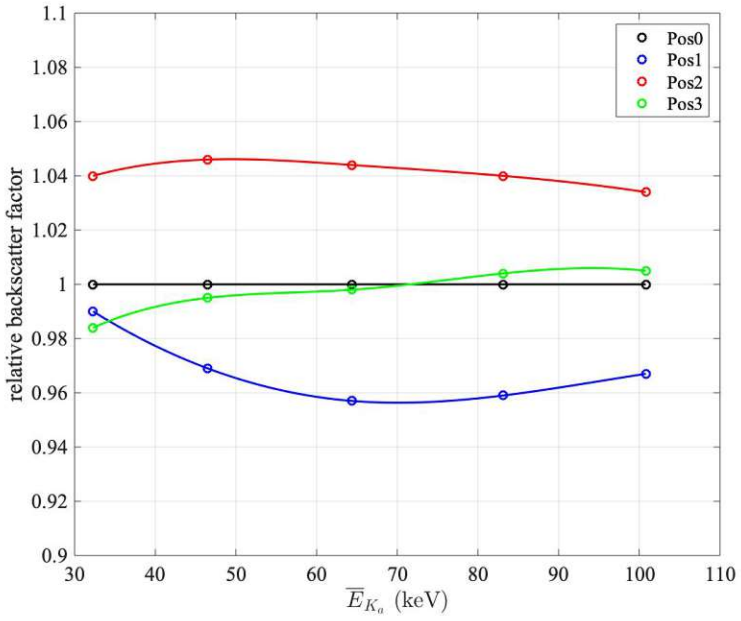

Figure 5.13: Relative backscatter factors as a function of the air kerma spectrum's mean energy $\overline{E}_{K_a}$ for three selected alternative positions of the SFD ('Pos1', 'Pos2' and 'Pos3'), with regard to the reference position ('Pos0').

this large distance from the focus. These results reflect one aspect of estimating measurement uncertainty in practical personal dosimetry.

5.7 Deviations in Measured Backscatter Factors for the SFD Depending on Choice of Phantom

The ISO slab was used as reference here since dosemeters are calibrated on this phantom now and in future, independent from the new definition of H_p. Deviations in measured backscatter factors on the Alderson phantom relative to the results for the ISO slab are vividly presented in Tab. 5.11 and Fig. 5.14 to Fig. 5.16

For all three angles of radiation incidence (0°, 30°, 60°) the same characteristic could be observed. For 23,7 keV almost no distinction in the backscatter factor can be made. Already at the next step (32,3 keV) it shows a significant higher backscattering on the Alderson. A dosemeter calibrated with this radiation quality on the ISO slab would receive increased H_p by about 3 % to 5 %, if the person carrying this dosemeter at the reference position had the same physical appearance as the Alderson. Interestingly, this effect reverses somewhere in the energy range between

46,5 keV and 64,4 keV. While the backscattering behavior of the two phantoms converges again for 46,5 keV, backscattering was slightly stronger on the ISO slab at 64,4 keV. A dosemeter would now underestimate H_p by up to 1 % to 2 %.

This tendency of reduced backscattering on the Alderson is kept for the whole series up to 120,6 keV and even becomes increasingly clear (3 % to 5 %). Therefore, personal monitoring under usage of dosemeters calibrated on the ISO slab is less conservative in this energy range.

However, it should be remembered that the differences found are specific for the SFD ionization chamber, which allows a general statement since its behavior is close to that of the ideal detector. A real dosemeter could have a different sensitivity with respect to backscatter.

radiation quality	$\overline{E}_{K_a}$ (keV)	$B_{\text{Alderson}}/B_{\text{Slab}}$ $\alpha = 0°$	$\alpha = 30°$	$\alpha = 60°$
N-30	23,7	-0,2 %	0,2 %	0,8 %
N-40	32,3	4,6 %	3,5 %	3,1 %
N-60	46,5	0,9 %	1,0 %	2,0 %
N-80	64,4	-1,9 %	-1,8 %	-1,0 %
N-100	83,1	-3,7 %	-3,6 %	-2,6 %
N-120	100,8	-3,3 %	-3,9 %	-2,9 %
N-150	120,6	-3,9 %	-4,7 %	-2,7 %

Table 5.11: Deviation in per cent of measured backscatter factors B_{Alderson} on the Alderson phantom relative to the backscatter factors B_{ISO} on the ISO water slab dependent on the angle of incidence α. $\overline{E}_{K_a}$ represents the air kerma spectrum's mean energy.

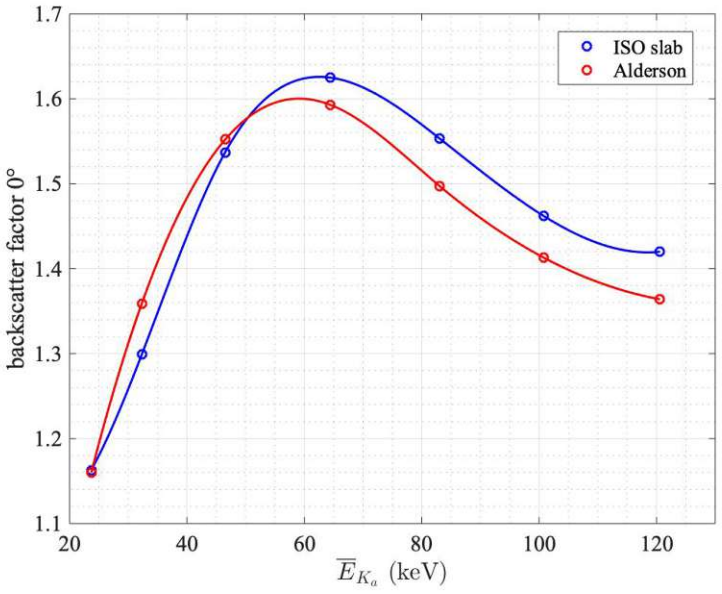

Figure 5.14: Comparison of measured backscatter factors on the ISO water slab or the Alderson phantom for perpendicular incidence of radiation.

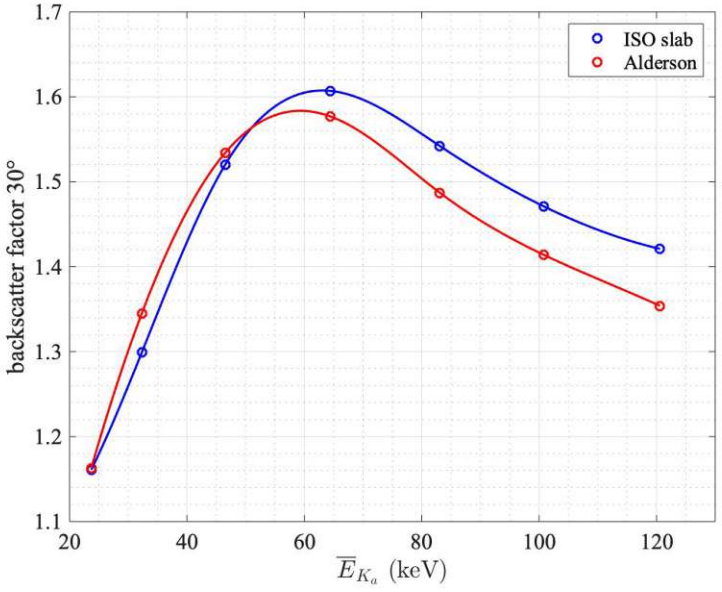

Figure 5.15: Comparison of measured backscatter factors on the ISO water slab or the Alderson phantom for an angle of incidence of 30°.

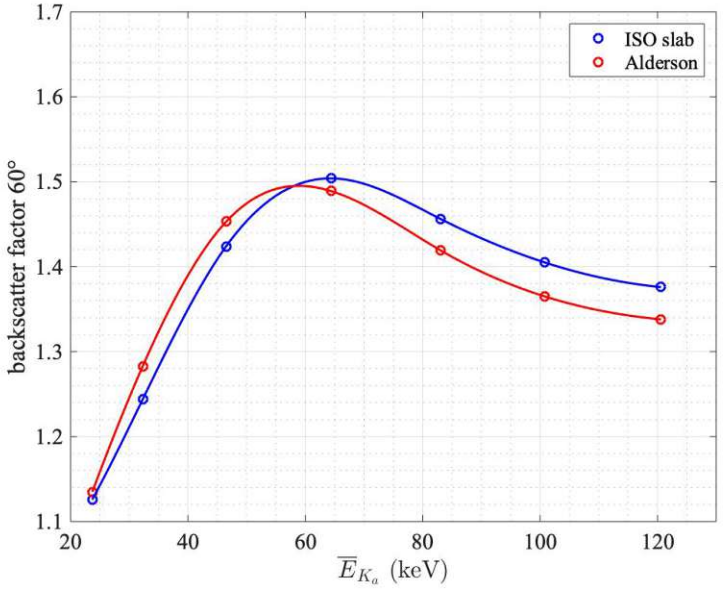

Figure 5.16: Comparison of measured backscatter factors on the ISO water slab or the Alderson phantom for an angle of incidence of 60°.

5.8 Response of the EPD and TLD on the ISO Slab and the Alderson

The EPD and the TLD system are calibrated to ^{137}Cs and thus the response on the ISO water slab is expected to be equal to one at 662 keV.

5.8.1 Response of the EPD

radiation quality	R_{Slab}	R_{Alderson}	$\frac{R_{\text{Slab}}}{R_{\text{Alderson}}}$
N-40	0,993	1,016	0,977
N-80	0,987	0,980	1,007
N-150	0,965	0,965	1,000

Table 5.12: $H_{\text{p}}(10)$ response A of the EPD, subdivided depending on the phantom to which they were attached (ISO slab or Alderson).

5.8.2 Response of the TLD

radiation quality	R_{Slab}	U	R_{Alderson}	U	$\frac{R_{\text{Slab}}}{R_{\text{Alderson}}}$
N-40	0,94	4,1 %	0,938	2,6 %	1,00
N-80	1,097	1,4 %	1,008	1,6 %	1,088
N-150	1,041	1,5 %	0,969	1,5 %	1,074

Table 5.13: $H_{\text{p}}(10)$ response of the TLD with expanded uncertainty $U(k = 2)$, subdivided depending on the phantom to which they were attached (ISO slab or Alderson).

5.8.3 Deviations in Measured Relative Response of the EPD and TLD Depending on Choice of Phantom

The two personal dosemeters show a quite different dependence from the phantoms they are attached to. In case of the EPD only at low energies a noticeable difference of +2,3 % in response can be seen when attached to the Alderson instead of the ISO slab. The deviation drops to -0,7 % for N-80, however, this difference is not significantly enough to attribute it solely to the change of phantom. For N-150, the choice of the phantom had no noticeable effect on the response. It can be concluded that the EPD is quite insensitive to backscattered radiation and therefore the influence of the phantom material and shape can be neglected for the EPD. Similarly, the real person's size and cloths will have no influence on the measurement results of the EPD.

The used TLD obviously didn't show such a flat energy dependence curve like the EPD and show a response of about 0,94 for both phantoms for N-40, therefore no distinction could be made. This is not the case for N-80 and N-150. Evaluated $H_{\text{p}}(10)$ dose is about 7 % to 9 % lower in case of irradiating the TLD attached on the Alderson phantom compared to the result for the ISO slab. TLD are thus more sensitive to backscatter radiation than EPDs and the SFD chamber. Usage of TLD attached to a real person with a similar physical appearance as the Alderson is therefore less conservative for these radiation qualities and will result in up to 10 % lower $H_{\text{p}}(10)$ values than expected by type testing on the calibration phantom. Nevertheless, these differences are within the required range of the energy dependence of the TLD.

in case of exactly the same irradiation as for the ISO slab serving as full-value substitute for the human torus.

5.9 Simulated Backscatter Factors on the Male MRCP

This research findings and related outcome is the result of using the mesh-type reference computational phantoms (MRCPs) provided by the Hanyang University Radiation Engineering Laboratory (HUREL) at Hanyang University in Seoul, Korea.

Results for the backscatter factors calculated on the MRCP are listed in Tab. 5.14. As discussed in Chap. 4, these results are not directly comparable to the results obtained for the ISO slab due to the complex surface structure of the MRCP and the variety of possible positions of the detector. However, the results appear to be consistent with the simulations and measurements discussed before.

radiation quality	B	U
N-30	1,191	0,4 %
N-40	1,351	0,7 %
N-60	1,568	1,0 %
N-80	1,651	1,1 %
N-100	1,605	1,0 %
N-120	1,558	0,9 %
N-150	1,461	0,7 %

Table 5.14: Simulated backscatter factors B on the male MRCP with expanded uncertainty $U(k = 2)$ for perpendicular incidence.

Chapter 6

Conclusion and Outlook

6.1 Significance of Research Findings

One of the central questions of this work was whether the ISO water slab phantom can continue to be used as dosemeter calibration phantom for the new measurand, the personal dose H_p, as it has been for $H_p(10)$ and $H_p(0,07)$ so far.

The personal dose is defined by the air kerma at a point on the surface of the human body multiplied with a conversion coefficient and is thus related to the backscatter factor. In the course of the Monte Carlo simulations, it was first shown that the SFD ionization chamber used in the measurements comes close to an ideal detector with respect to the determination of the air kerma and the backscatter factor. Therefore the SFD represents a suitable tool for determining the backscatter factor and its dependence on the phantom geometry.

From the results of the measurements of the backscatter factor on the ISO water slab and on the anthropomorphic Alderson phantom, it could be concluded that the difference in the shape of the phantoms had only an insignificant effect, roughly ± 5 %. Similarly, for an electronic personal dosemeter (EPD) as well as for thermoluminescent dosemeters (TLD), both commonly used $H_p(10)$-dosemeters, variations in their relative response dependent on the phantom they were applied to were in an acceptable range and did not imply any serious deficiencies regarding the usability of the ISO water slab.

The deviations found represent a reasonable margin in practical radiation protection. Thus, maintaining on the previously used calibration phantom for the new measurand H_p could be confirmed in the photon energy range of radiation qualities commonly used in mammography and diagnostics. It is therefore not necessary to design a new phantom commonly used in radiation protection applications that is closer to the human body.

The recommendations of ICRP report 95 [2] are thus supported by our results since it could be shown that the ISO water slab represents the real human body to the fullest satisfaction with regard to the requirements in practical radiation protection.

Beside the difference in geometric shape between the real human body and the calibration phantom, additional uncertainty contributions in practical personal dosimetry arise from the manner the person carries the dosemeter. Varying the dosemeter carrying position on the thorax by a few centimeters influences the measurement result to the same or even greater extent as the difference arising from the choice of the phantom used for backscatter measurements. This was shown in the measurements of the relative backscatter factors on the Alderson phantom.

Results for the measured backscatter factors on the ISO water slab, the Alderson phantom as well as the simulated backscatter factors on the ISO water slab and the male MRCP serve as reference values for future projects in this field.

6.2 Measuring Devices in Future

In the following, we assume that the normative requirements on dosemeters will remain the same once the ICRU 95 [2] proposals of the new operational quantities are legally binding. So far, such requirements are specified in following international standards from the International Electrotechnical Commission (IEC): IEC 60846 [29, 30], IEC 61526 [31], IEC 62387 [32] and IEC 61005 [33].

The procedure discussed below can be carried out for a dosemeter assessing any operational dose quantity. To evaluate whether a dosemeter intended to measure an 'old' operational dose quantity (according to ICRU report 39/51 [3, 4]) can be used for measurement of the corresponding 'new' operational dose quantity (according to ICRU report 95), the quotient of the 'old' conversion coefficient h_{old} to the 'new' conversion coefficient h can be applied on, for example, the response R_{old} with regard to the old quantities

$$R = \frac{h_{\mathrm{old}}}{h} \cdot R_{\mathrm{old}} \tag{6.2.1}$$

The result is the response R with regard to the new quantities [2].

If the relative response R/R_0 (for example relative to the response R_0 for radiation quality S-Cs of the radionuclide ^{137}Cs at 0° reference angle of radiation incidence) of the dosemeter lies within the limits specified in the corresponding standards, usually between $(R/R_0)^{\mathrm{min}} = 0,71$ and $(R/R_0)^{\mathrm{max}} = 1,67$ for the quantity $H_{\mathrm{p}}(10)$, after the transformation (Equ. 6.2.1) to the new quantities, it can be

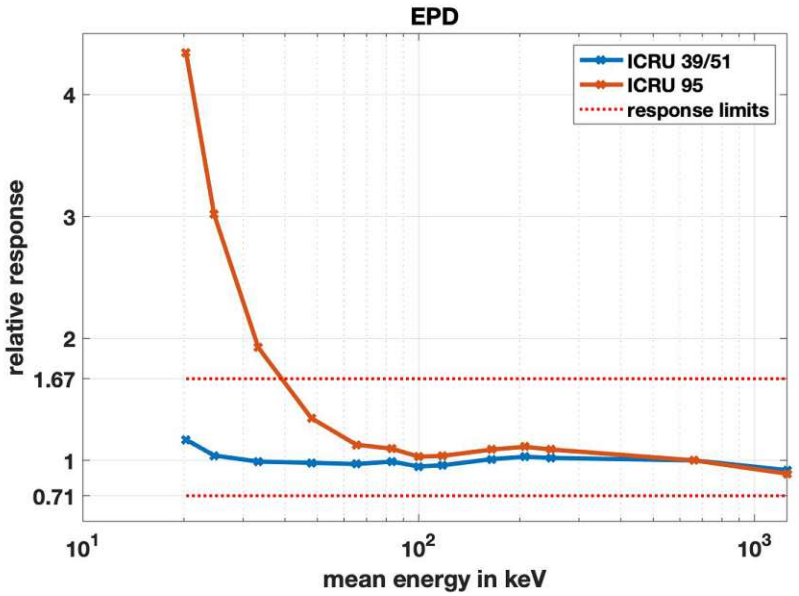

Figure 6.1: Response relative to that at 662 keV of the electronic personal dosemeter (EPD) with regard to the operational dose quantities according to ICRU report 39/51 [3, 4] and ICRU report 95 [2]. Conversion coefficients for the ICRU 39/51 quantities were taken from [21], those for the ICRU 95 quantities from [34].

used without any modifications on the device. Solely the calibration in terms of the new quantity has to be carried out to obtain the value for the response R_0 at reference conditions.

6.2.1 Examples

The impact of the introduction of the new operational dose quantities on their response was considered for selected dosemeters.

Personal Dosemeter: EPD The energy dependence of the $H_p(10)$-response of the electronic personal dosemeter (EPD) used in the measurements described in the previous chapters was measured. Obviously, the EPD fulfills the requirements on measurement of the old operational dose quantities specified in IEC 61526:2010.

Transforming the response according to Equ. 6.2.1 gives the response with regard to the 'new' quantity, the personal dose H_p. Both is then divided by the corresponding value for the response at 662 keV (S-Cs) which gives the relative response (Fig. 6.1). Response limits at 0° are exceeded at photon energies below 50 keV for the assessment of H_p.

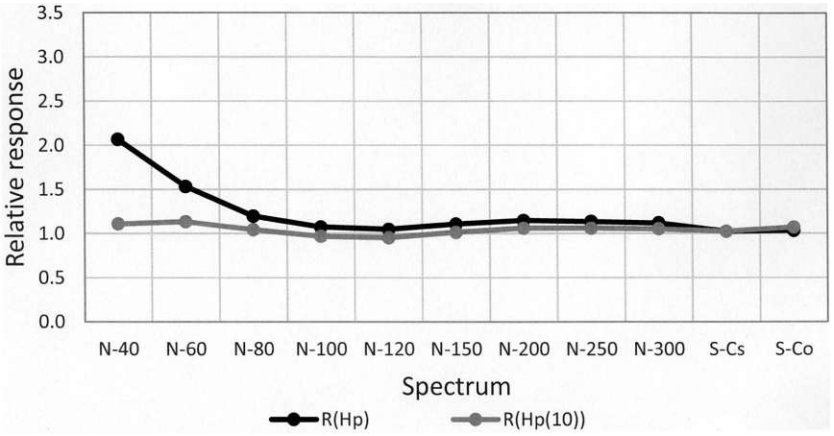

Figure 6.2: Response relative to that at 662 keV of TLD [35] with regard to the operational dose quantities according to ICRU 39/51 [3, 4] and ICRU 95 [2].

Personal Dosemeter: TLD Considering the energy dependence of the $H_{\mathrm{p}}(10)$-response of whole-body thermoluminescent dosemeters (TLD, Harshaw Type 8840 based on LiF:Mg,Cu,P), taken from [35], it can be seen that the TLD fulfill the requirements for personal dosemeters specified in IEC 61526:2010 (Fig. 6.2). Nevertheless, the TLD over-response significantly in the low-energy regime when assessing H_{p} which coincidences witch other research findings [36, 37]. Here it also could be found that the uncovered element of multi-element TLD for assessment of $H_{\mathrm{p}}(0,07)$ for its own delivers quiet unaffected results and give a good estimate of the new quantity $D_{\mathrm{local\,skin}}$ due to the very similar definition. Thus, in principle, the requirements could be met by adjusting the evaluation algorithm. Else, a redesign of TLD will be necessary to provide truly satisfactory results for H_{p}. This will probably be true to a similar extent for most passive personal dosemeters optimized for personal dose equivalent [35].

Area Dosemeter Data for the relative response of a typical dosemeter intended to measure ambient dose equivalent $H^*(10)$, a 'SSM1+' with integrated counter tubes fabricated by Seibersdorf Labor GmbH, were available. Applying the same procedure as before allows the conversion of the $H^*(10)$-response to H^*-response (Fig. 6.3). In this case it is obvious that the response is quite unaffected since the changes in conversion coefficients are relatively small in the energy range relevant for this dosemeter. This is valid for most survey measuring devices which show an energy cutoff below approximately 50 keV photon energy, which allows a standard calibration in terms of the new quantity without the need of a redesign [35, 37].

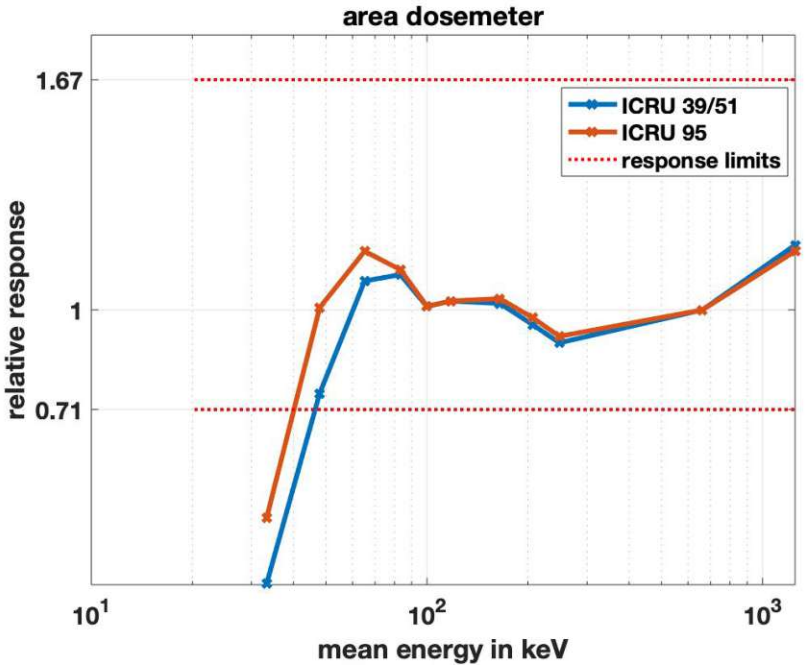

Figure 6.3: Response relative to that at 662 keV of an area dosemeter (SSM1+) with regard to the operational dose quantities according to ICRU 39/51 [3, 4] and ICRU 95 [2]. Conversion coefficients for the ICRU 39/51 quantities were taken from [21], those for the ICRU 95 quantities from [34].

Acknowledgements

First and foremost, I would like to thank my supervisor from the Vienna University of Technology and former head of department at the Federal Office of Metrology and Surveying (BEV), Prof. Dr. Franz Josef Maringer, for his exceedingly friendly responsiveness throughout the entire time of working on this thesis, from planning to completion and probably beyond. Not only from the start of this work, but also before, one could always trust in his advice and always found support with all concerns.

A big thank you to my supervisor from Seibersdorf Labor GmbH, Dr. Christian Hranitzky, who has shown an unbelievable degree of helpfulness and technical competence. As a friendly colleague as well as an instructor, he has invested a lot of time, even during his vacations, to bring me closer to MCNP and scientific working and to bring this diploma thesis to a high technical level.

I would like to thank Dipl.-Ing. David Sorger from the Dosimeterservice of Seibersdorf Labor GmbH for the organization, the joint measurements and the evaluation of the TLD measurements.

A big thanks to my good friend, Felix Schlaffer, B.Sc., for making the drawing of the model of the SFD ionization chamber.

I would like to thank the dosimetry laboratory of the International Atomic Energy Agency, especially Ladislav Czap, M.Sc., for kindly providing the Alderson phantom.

Bibliography

[1] *Radiation protection – Terms and definitions to ionising radiation*, ÖNORM A 6601:2012-03-15, Austrian Standards Institute, 2012.

[2] *Operational Quantities for External Radiation Exposure*, ICRU Report 95, International Commission on Radiation Units and Measurements, 2020.

[3] *Determination of Dose Equivalents Resulting from External Radiation Source*, ICRU Report 39, International Commission on Radiation Units and Measurements, 1985.

[4] *Quantities and Units in Radiation Protection Dosimetry*, ICRU Report 51, International Commission on Radiation Units and Measurements, 1993.

[5] H. Krieger, *Grundlagen der Stahlenphysik und des Strahlenschutzes*, 6th ed. Springer, 2019.

[6] J. Als-Nielsen and D. McMorrow, *Elements of Modern X-ray Physics*, 2nd ed. Wiley, 2011.

[7] J. E. Turner, *Atoms, Radiation, and Radiation Protection*, 3rd ed. Wiley, 2007.

[8] *Patient Dosimetry for X Rays used in Medical Imaging*, ICRU Report 74, International Commission on Radiation Units and Measurements, 2005.

[9] *Dosimetry in Diagnostic Radiology: An International Code of Practice*, Technical reports series no. 457, International Atomic Energy Agency, 2007.

[10] *Key Data for Ionizing-Radiation Dosimetry: Measurement Standards and Applications*, ICRU Report 90, International Commission on Radiation Units and Measurements, 2016.

[11] H. Krieger, *Strahlungsmessung und Dosimetrie*, 2nd ed. Springer Spektrum, 2013.

[12] *The 2007 Recommendations of the International Commission on Radiological Protection*, ICRP Publication 110, International Commission on Radiological Protection, 2007.

[13] T. Otto, "Conversion coefficients from kerma to ambient dose and personal dose for X-ray spectra," *Journal of Instrumentation*, vol. 14, no. 11, pp. 11 011–11 011, 2019.

[14] R. Behrens and G. Dietze, "Dose conversion coefficients for photon exposure of the human eye lens," *Physics in Medicine & Biology*, no. 56, pp. 415–437, 2011.

[15] *Adult Reference Computational Phantoms*, ICRP Publication 110, International Commission on Radiological Protection, 2009.

[16] *Basic Anatomical and Physiological Data for Use in Radiological Protection: Reference Values*, ICRP Publication 98, International Commission on Radiological Protection, 2002.

[17] D. P. Landau and K. Binder, *A Guide to Monte Carlo Simulations in Statistical Physics*, 2nd ed. Cambridge University Press, 2005.

[18] *MCNP – A General Monte Carlo N-Particle Transport Code, Version 5*, LA-UR-03-1987, Los Alamos National Laboratory, NM, USA, 2008.

[19] *Radiological protection — X and gamma reference radiation for calibrating dosemeters and doserate meters and for determining their response as a function of photon energy — Part 1: Radiation characteristics and production methods*, ISO 4037-1, International Organisation of Standardization, 2019.

[20] C. Hranitzky, *DEL Spektrenkatalog – Röntgenstrahlungsqualitäten im Dosimetrielabor Seibersdorf*, 1st ed., Report SL-LD-007/2020, Seibersdorf Labor GmbH, 2020.

[21] *Radiological protection — X and gamma reference radiation for calibrating dosemeters and doserate meters and for determining their response as a function of photon energy — Part 3: Calibration of area and personal dosemeters and the measurement of their response as a function of energy and angle of incidence*, ISO 4037-3, International Organisation of Standardization, 2019.

[22] *MCNP Users Manual - Code Version 6.2*, LA-UR-17-29981, Los Alamos National Laboratory, NM, USA, 2017.

[23] *Adult Mesh-type Reference Computational Phantoms*, ICRP Publication 145, International Commission on Radiological Protection, 2020.

[24] C. Kim, Y. Yeom, T. Nguyen, M. Han, C. Choi, H. Lee, H. Han, B. Shin, J.-K. Lee, H. Kim, M. Zankl, N. Petoussi-Henss, W. Bolch, C. Lee, B. Chung, R. Qiu, and K. Eckerman, "New mesh-type phantoms and their dosimetric applications, including emergencies," *SAGE*, vol. 47, pp. 45–62, 2018.

[25] *Conversion Coefficients for use in Radiological Protection against External Radiation*, ICRP Publication 74, International Commission on Radiological Protection, 1996.

[26] H. Benmakhlouf, H. Bouchard, A. Fransson, and P. Andreo, "Backscatter factors and mass energy-absorption coefficient ratios for diagnostic radiology dosimetry," *Physics in Medicine & Biology*, vol. 56, pp. 7179–7204, 2011.

[27] N. Petoussi-Henss, M. Zankl, G. Drexler, W. Panzer, and D. Regulla, "Calculation of backscatter factors for diagnostic radiology using Monte Carlo methods," *Physics in Medicine & Biology*, vol. 43, no. 8, pp. 2237–2250, 1998.

[28] R. J. Traub, J. C. McDonald, and M. K. Murphy, "Determination of photon backscatter from several calibration phantoms," *Radiation Protection Dosimetry*, vol. 74, no. 1/2, pp. 13–20, 1997.

[29] *Radiation protection instrumentation - Ambient and/or directional dose equivalent (rate) meters and/or monitors for beta, X and gamma radiation - Part 1: Portable workplace and environmental meters and monitors*, 1st ed., IEC 60846-1, International Electrotechnical Commission, 2009.

[30] *Radiation protection instrumentation - Ambient and/or directional dose equivalent (rate) meters and/or monitors for beta, X and gamma radiation - Part 2: High range beta and photon dose and dose rate portable instruments for emergency radiation protection purposes*, 2nd ed., IEC 60846-2, International Electrotechnical Commission, 2015.

[31] *Radiation protection instrumentation - Measurement of personal dose equivalents Hp(10) and Hp(0,07) for X, gamma, neutron and beta radiations - Direct reading personal dose equivalent meters*, 3rd ed., IEC 61526, International Electrotechnical Commission, 2010.

[32] *Radiation protection instrumentation - Dosimetry systems with integrating passive detectors for individual, workplace and environmental monitoring of photon*

and beta radiation, 2nd ed., IEC 62387, International Electrotechnical Commission, 2020.

[33] *Radiation protection instrumentation - Neutron ambient dose equivalent (rate) meters*, 3rd ed., IEC 61005, International Electrotechnical Commission, 2014.

[34] R. Behrens and T. Otto, "Conversion coefficients from total air kerma to the newly proposed ICRU/ICRP operational quantities for radiation protection for photon reference radiation qualities," *Journal of Radiological Protection, in press*, 2020.

[35] D. Ekendahl, Z. Ĉemusová, D. Kurková, and M. Kapuciánová, "Response of current photon personal dosemeters to new operational quantities," *Radiation Protection Dosimetry*, vol. 190, no. 1, pp. 45–57, 2020.

[36] J. S. Eakins and R. J. Tanner, "The effects of revised operational dose quantities on the response characteristics of a beta/gamma personal dosemeter," *Journal of Radiological Protection*, vol. 39, no. 2, pp. 399–421, 2019.

[37] T. Otto, "Response of photon dosimeters and survey instruments to new operational quantities proposed by icru rc26," *Journal of Instrumentation*, vol. 14, no. 1, pp. 1010–1010, 2019.

[38] *Evaluation of measurement data - Guide to the expression of uncertainty in measurement*, JCGM 100:2008, Joint Committee for Guides in Metrology.

[39] *User Manual: SFD Chambers Type 34060 and Type 34069*, D781.131.00/01, PTW-Freiburg, Freiburg, DE, 2008.

Appendices

Appendix A

Estimation of Uncertainty in Measurements and Simulations

A.1 Experimental Results

Uncertainty was estimated considering the recommendations of the 'Evaluation of measurement data – Guide to the expression of uncertainty in measurement' [38].

Specified uncertainties for the results in Chap. 5 where solely derived from statistical considerations of the measurements concerned.

A.1.1 1. Standard Uncertainty of Average of Several Data Points

Each data point for an ionization current represents the arithmetic mean I of single measurements of ionization currents I_i:

$$I = \frac{1}{n} \cdot \sum_i I_i \tag{A.1.1}$$

n is the number of measurements, which was three in our case due to the relatively long measurement durations between 150 and 300 seconds. The experimental standard deviation $s(I)$ of the current I is given by

$$s(I) = \sqrt{\frac{\sum_i (I_i - I)^2}{n-1}} \tag{A.1.2}$$

Dividing $s(I)$ by the square root of the number of measurements delivers the standard uncertainty of the measured ionization current I for normally distributed I_i, which is equal to the expanded uncertainty with the coverage factor $k = 1$ corre-

sponding to a level of confidence of 68,27 %. Since the number of measurements was limited to $n = 3$, a student's t-distribution was assumed. The degree of freedom required for the determination of the two-sided t-value for the desired level of confidence of 68,27 % is given by $\nu = n - 1$. Thus the standard uncertainty $u_1(I)$ results in

$$u_1(I) = t_{\mathrm{P}}(\nu) \cdot \frac{1}{\sqrt{n}} \cdot s(I) \tag{A.1.3}$$

A.1.2 2. Standard Uncertainty of Single Data Points

The relative standard uncertainty $u(I_i)$ of the measured ionization currents I_i of the monitor and the SFD for every single measurement was calculated by the measurement program and included the relative standard deviation of the current and the uncertainty of the capacitance of the used capacitors and of the correction with regard to air density. The standard uncertainty of the arithmetic mean I (Equ. A.1.1) can therefore be expressed as combined standard uncertainty according to the uncertainty propagation law

$$u_2(I) = \sqrt{\sum_i \left(\frac{\partial I}{\partial I_i}\right)^2 \cdot u^2(I_i)} \tag{A.1.4}$$

Since the measurement program calculates I_i stepwise for every second and all measurement times were over 150 seconds, a normal distribution could be assumed.

A.1.3 Complete Expanded Uncertainty of the Ionization Current

The combined standard uncertainty $u_{\mathrm{c}}(I)$ of a measured ionization current I evaluated as arithmetic mean of three single measurements of ionization currents I_i was calculated by

$$u_{\mathrm{c}}(I) = \sqrt{u_1^2 + u_2^2} \tag{A.1.5}$$

Applying a coverage factor of $k = 2$ on $u_{\mathrm{c}}(I)$ gives the expanded uncertainty $U(I)$ corresponding to a level of confidence of 95 %:

$$U(I) = 2 \cdot \sqrt{u_{\mathrm{c}}^2(I)} \tag{A.1.6}$$

Since the irradiation time for each single measurement was chosen to result $u(I_i)$ for the SFD to be smaller than 0,03 % (the uncertainty in the monitor current is always small compared to the SFD), $u_2(I)$ could have been neglected and thus only

the standard deviation of the arithmetic mean of the data points could have been included in the calculation. In case of the monitor which is close to the focus this approach is definitely applicable since it receives a high dose rate and therefore small u_2. For I_i measured using the SFD, this is not necessarily the case. Equ. A.1.5 was applied for all measured ionization currents.

A.1.4 Uncertainty of the Backscatter Factor

The backscatter factor $b(\alpha)$ was evaluated by reduction of Equ. 2.2.13 to

$$b = \frac{I_{\mathrm{C}}/I_{\mathrm{M}}}{I_{\mathrm{C,ph}}/I_{\mathrm{M,ph}}} \tag{A.1.7}$$

where 'C' and 'C,ph' refer to the chamber current in case of absence or in presence of the phantom, respectively. This applies analogously to the monitor current ('M' and 'M,ph').

In the following, 'X' represents the indices 'M', 'M,ph', 'C', 'C,ph'. Equ. A.1.7 represents the model function from which the combined standard uncertainty $u_{\mathrm{c}}(b)$ could be calculated by

$$u_{\mathrm{c}}(b) = \sqrt{\sum_{\mathrm{X}} \left(\frac{\partial b}{\partial I_{\mathrm{X}}}\right)^2 \cdot u^2(I_{\mathrm{X}})} \tag{A.1.8}$$

The expanded uncertainty with coverage factor $k = 2$ is thus given by

$$U(b) = 2 \cdot u_{\mathrm{c}} \tag{A.1.9}$$

$u(I_{\mathrm{X}})$ was evaluated using Equ. A.1.5. The procedure for the evaluation of estimated expanded uncertainty of the relative backscatter factor (Sec. 5.6.2) is analogous.

A.1.5 Non-Quantified Uncertainty in SFD Measurements

For reproducibility reasons, the experimental setups were rebuilt and comparison measurements of the backscatter factor or rather the SFD chamber factor were carried out. The aim of these measurements was to obtain an estimate of the margin of deviations in measured backscatter factors and air kerma using the SFD resulting from slightly different positioning of the SFD and the phantoms (distance from focus, angles) and unknown varying parameters in the measurement system. These influences were not quantified, but naturally led to deviations when repeating measurements which are not paid attention by the statistic uncertainties discussed be-

fore. All results were within the regarding expanded uncertainty pointed out before. Thus, non-quantified uncertainty contributions are expected to be not dominant compared to the pure statistical margin.

A.1.6 Uncertainty of Response Measurements (TLD, EPD)

The expanded uncertainty of the mean equivalent dose of the irradiated TLD for each setup was calculated in the same way as for the average of several average ionization currents. On each standard uncertainty u the corresponding t-value dependent on the number of TLD and corresponding to 68,27 % coverage probability was multiplied. Applying a coverage factor $k = 2$ on u gives the expanded uncertainty U.

Results from the EPD were adopted unchanged without estimation of uncertainty, since these measurements served as exemplary re-enactment of a situation that may occur in practical radiation protection where an EPD is used to obtain a fast result.

A.2 Computational Results

For each calculated MCNP tally, the estimated relative standard uncertainty $u_{\overline{x}}$ of the mean $\overline{x}$, the quantity which is tallied, representing the statistical precision is printed out. As discussed in Chap. 2, for a well behaved tally $u_{\overline{x}}$ is dependent on the number of histories, n, through the relation

$$R \propto \frac{1}{\sqrt{n}} \tag{A.2.1}$$

According to the central limit theorem, for $n \to \infty$, the chance that the tally result is in the range $\overline{x}(1 \pm 2u_{\overline{x}})$ is 95 % [18]. Therefore, the expanded uncertainty $U(k = 2)$ can be written as

$$U(\overline{x}) = 2 \cdot u_{\overline{x}} \tag{A.2.2}$$

This statement is regarding the precision of the Monte Carlo simulation, not regarding the accuracy of the result and its physical interpretation and is actually empirically found knowledge. Thus, if one uses R to obtain a confidence interval about the estimated mean and therewith form a confidence interval about the interpreted physical result, sampling techniques, approximations, uncertainties in physical data etc have to be taken into account additionally. A Monte Carlo simulation is always just an idealization of a real situation and its accuracy can just be confirmed in a

certain extent by comparison with the experiment.

U in this context is the statistical precision of the calculated tally interpreted as the expanded uncertainty (k=2) and is given together with the results for the simulation considered.

Combination of two tally results as it is the case for the calculation of the conversion factor and the backscatter factor is straightforward and analogous to the procedure in Sec. A.1. The model functions were discussed in Sec. 4

Appendix B

SFD Chamber Type 34069 Geometry

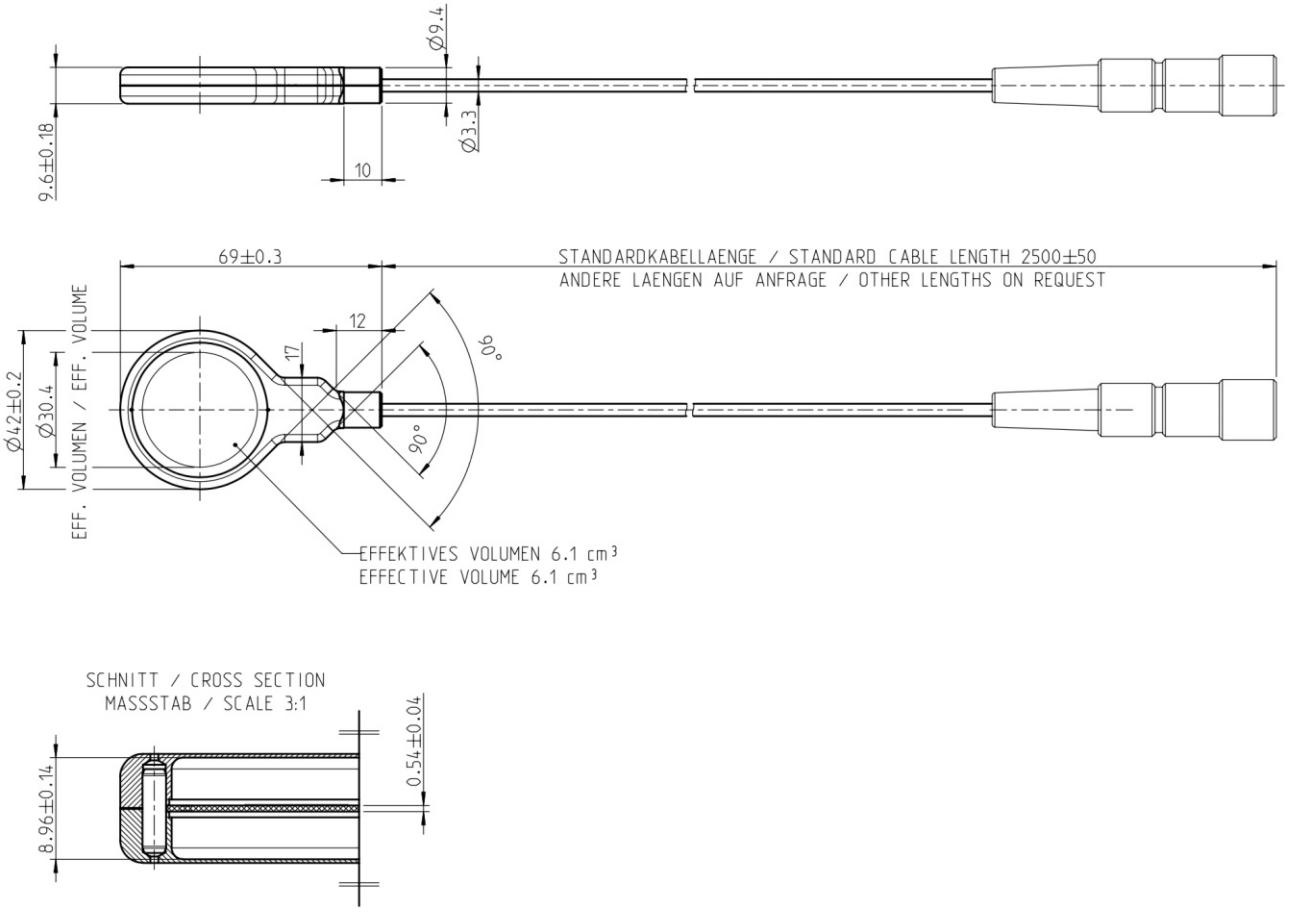

Figure B.1: Detailed drawing of the SFD chamber type 34069 [39].